

# Reexamining constraints on neutron star properties from perturbative QCD

Dake Zhou<sup>1,2,3,4,\*</sup>

<sup>1</sup>*Department of Physics, University of Washington, Seattle, WA 98195*

<sup>2</sup>*Institute for Nuclear Theory, University of Washington, Seattle, WA 98195*

<sup>3</sup>*Department of Physics, University of California Berkeley, Berkeley, CA 94720*

<sup>4</sup>*Department of Physics and Astronomy, Northwestern University, Evanston, IL 60208*

(Dated: December 24, 2024)

The implications of perturbative QCD (pQCD) calculations on neutron stars are carefully examined. While pQCD calculations above baryon chemical potentials  $\mu_B \simeq 2.4$  GeV demonstrate the potential of ruling out a wide range of neutron star equations of state (EOSs), such constraints only affect the most massive neutron stars in the vicinity of the Tolman-Oppenheimer-Volkoff (TOV) limit, resulting in constraints that are orthogonal to current or expected astrophysical bounds. In the most constraining scenario, pQCD considerations favor low values of the squared speed of sound  $C_s$  at high  $\mu_B$  relevant for the most massive neutron stars, but leave predictions of the radii and tidal deformabilities almost unchanged. Such considerations become irrelevant if the maximum speed of sound squared inside neutron stars does not exceed about  $C_{s,\max} \simeq 0.5$ , or if pQCD breaks down below  $\mu_B \simeq 2.9$  GeV. Furthermore, the large pQCD uncertainties preclude any meaningful bounds on the neutron star EOS at the moment. Interestingly, if pQCD predictions for the pressure at around  $\mu_B \simeq 2.5$  GeV are refined and found to be low ( $\lesssim 1.5$  GeV/fm<sup>3</sup>), evidence for a soft neutron star inner core EOS in combination with the existence of two-solar-mass pulsars would indicate the presence of color superconductivity beyond neutron star densities. I point out that two-solar-mass pulsars place robust upper bounds on this non-perturbative effect and require the pairing gap to be less than  $\Delta_{\text{CFL}} \leq 500$  MeV at  $\mu_B \simeq 2.5$  GeV.

## I. INTRODUCTION

An *ab initio* QCD-based calculation of dense matter beyond a few times the nuclear saturation density ( $n_0 = 0.16$  fm<sup>-3</sup>) relevant for the interior of neutron stars remains challenging. This strongly interacting regime not only precludes perturbative calculations but also discourages applications of lattice methods due to the sign problem [1–3]. Such obstacles have deprived us of a clear understanding of neutron stars even though almost a century has passed since their conception by Landau and by Zwicky and Baade [4].

In contrast to the stagnation in this strongly coupled region, significant progress has been made at the low- and ultra-high-density frontiers. On one hand, for baryon number densities below about  $\simeq 2n_0$ , an effective description based on symmetries of QCD has proven fruitful in predicting the properties of neutron-rich matter. Dubbed chiral effective field theory ( $\chi$ EFT) [5–12], it allows for and arranges all possible operators respecting chiral symmetry through a power counting scheme [8, 10]. The result is a systematic expansion in nucleon momenta that not only enables calculations of the equations of state but also provides error estimates through order-by-order comparisons [13–18]. For example, the recent next-to-next-to-next leading order (N<sup>3</sup>LO) calculation reveals that the  $1\sigma$  uncertainties associated with the pressure of pure neutron matter (PNM) to be  $\approx 10\%$  at  $n_B = n_0$ , and worsen to about  $40\%$  at  $2n_0$  [18]. On the other hand, at densities above  $\simeq 30 - 50n_0$ , asymptotic freedom of

QCD suggests perturbative treatments become valid and useful. The pioneering work of [19, 20] confirmed that cold quark matter resembles closely to a Fermi gas in this region, and has promoted significant efforts in simplifying and improving calculations for cold and dense QCD [21–25].

Given the scarcity of available information directly related to the phase of matter at supranuclear densities in between, gleaming as many insights as possible from both ends is a desirable undertaking. That high-density pQCD calculations may place limits on NS EOSs through thermodynamic consistency requirements is well-known, and there is only a potential for constraints because the current uncertainties associated with pQCD predictions are simply too large to place meaningful bounds. However, a renewed wave of interest in this topic is recently generated by [26]. That letter along with the subsequent papers [27] including attempts to clarify it [28] implicitly made several yet to be justified assumptions and have led to apparently widespread misunderstandings in the literature.

In this first paper of the series exploring the interplay between high- and low-density theoretical inputs I focus on the implications of pQCD calculations on neutron stars and the underlying EOS. One objective is to clarify the misunderstandings on this subject. Specifically, it will be shown that due to the undetermined strength of non-perturbative effects only one type of the bounds derived from thermodynamic relations may be viewed as a constraint on NS EOSs. Furthermore, while pQCD constraints do demonstrate the potential of ruling out a considerable region in the EOS space, astrophysical observables are barely affected by these high-density inputs, as

\* dkzhou@berkeley.edu

bounds from pQCD are mostly orthogonal to those from astrophysics.

The rest of the paper is organized as follows. A simple parameterization of  $\chi$ EFT EOSs is discussed in section II, and the pQCD EOS for cold quark matter is reviewed in section III. In section IV I review the previously-known model-independent bounds on the pressure that the low- and high-density EOSs must satisfy [29–32]. In section V I apply these bounds and carefully examine the underlying assumptions, the applicable ranges, and their consequences. Main results and future directions are summarized in section VI. Throughout the discussion I adopt the natural unit system in which  $G = \hbar = c = 1$ .

## II. NEUTRON STAR EOS

In this section I give an overview of the parameterization of neutron star EOSs used in this work. Some details are reported in [33, 35].

### A. parameterizing $\chi$ EFT-based EOSs with correlated uncertainties

Recently, refs [18, 34] studied truncation errors of  $\chi$ EFT based on the assumptions that its predictions for energy per particle admit a polynomial expansion in momenta, and that the unknown coefficients associated with higher order terms are natural in size. Using a Gaussian Process (GP) interpolant the authors inferred the size and characteristic length scales of the inter-density correlations of the polynomial coefficients, and used these to obtain extrapolated truncation errors. The resulting correlated uncertainties are encoded in the covariance matrix  $\text{Cov}(E_i, E_j)$  where  $E_{i,j}$  are energies per particle at the  $i$ th and  $j$ th tabulated density points, excluding the rest mass. Although one can reconstruct the GP interpolant reported there and use it to generate EOS samples, this approach may not be easily extended to construct beta-equilibrium EOSs that respect the underlying inter-density correlations.

Here, I present a minimal, faithful parameterization of the  $\chi$ EFT calculations that captures not only the central values but also the correlated truncation errors. The type of correlation I focus on is the inter-density correlation, as it is the most significant one in approach to describe the beta-equilibrium neutron-rich matter, to be discussed below. For a discussion on the correlation between pure neutron matter (PNM) and symmetric nuclear matter (SNM) EOSs, see [18, 32]. At the core of this parameterization lies the eigenvalue decomposition (singular value decomposition) of the covariance matrix

$$USU^T = \|\text{Cov}(E_i, E_j)\|. \quad (1)$$

The eigenvectors in  $U$  are orthonormal since the covariance is symmetric. In particular, each eigenvector  $U_i$

represents a correlation among different densities of the truncation error, with the  $1\sigma$  variance given by the square root of its corresponding eigenvalue  $\sqrt{\text{diag}(S)_i}$ . For both the chiral potentials with 450 MeV and 500 MeV cutoffs reported in [18], the largest (second largest) entry in  $\sqrt{\text{diag}(S)}$  accounts for about 90% (8%) of the variances encoded in the full covariance matrix, suggesting their corresponding eigenvectors, which shall be referred to as the most significant eigenvectors, are adequate for current and future astrophysical applications. This procedure is suitable for both PNM and SNM calculations, and for concreteness let us focus on the PNM EOS of the form  $E(n_n)$  where  $n_n$  is the neutron number density.

The two most significant eigenvectors form a set of orthogonal basis to describe the correlated uncertainties. Denote  $E_0(n_n)$  the central values of energy per particle predicted by  $\chi$ EFT, the proposed parameterization that incorporates correlated uncertainties takes the form

$$\begin{aligned} \widehat{E}(n_n) &= \widehat{E}_0(n_n) + \sum_{i=1}^2 a_i \widehat{E}_i(n_n) + m_n, \\ &\text{with } \widehat{E}_i(n_n) = \sqrt{\text{diag}(S)_i} U_i(n_n). \end{aligned} \quad (2)$$

Above,  $m_n$  is the mass of neutron. The variance associated with each eigenvector is absorbed into the definition of basis functions  $\widehat{E}_i(n_n)$ , so that the (uncorrelated) coefficients  $a_i$  are independent identical draws from the standard normal distribution  $\mathcal{N}(0, 1)$ . This procedure effectively projects out the high-dimensional covariance matrix to a lower dimension subspace spanned by the basis functions  $\widehat{E}_{i=1,2}(n_n)$ .

These basis functions, along with the central values  $E_0(n_n)$ , are well-behaved and can be faithfully represented by polynomials. For optimal fittings, polynomials of degree  $\gtrsim 5$  are sufficient as the fitted EOS as well as derivatives are stationary with increasing polynomial degrees. This allows us to turn the discrete tabulated EOS from  $\chi$ EFT calculations to a compact, faithful, and continuous representation eq. 2. The resulting EOSs in this parameterization are shown in fig. 1. The pressure follows from the thermodynamic relation  $P = n_n^2 (dE/dn_n)$ , and the  $1\sigma$  upper and lower bounds of correlated errors are obtained by setting  $a_1 = a_2 = \pm 1$  in eq. 2. For comparison, the uncorrelated  $1\sigma$  errors obtained by taking the square root of  $\text{diag}(\|\text{Cov}(E_i, E_j)\|)$  are shown as the blue band. The importance of inter-density correlations is evident as the boundaries of the blue band underestimate the error in pressure by almost 1/3 near  $n_B = 2n_0$ . Inter-density correlations are positive since the energy at a given point is less likely to be low if its neighboring points are predicted to have high energies by the chiral interaction.

The EOS in eq. 2 can be parameterized either against number densities  $n_n$  or Fermi momenta  $k_F$ . The covariance matrix obtained in [18] in fact involves  $E(k_F)$  tabulated on an equally spaced grid in Fermi momenta  $k_F$ , as inter-density correlations appear more natural on this

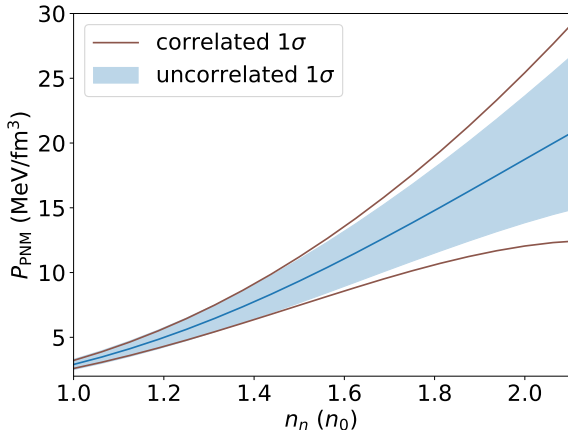


FIG. 1. The pressure of the PNM along with  $1\sigma$  uncertainties from  $\chi$ EFT calculations at N3LO. This EOS is based on the chiral potential with a 500 MeV cutoff reported in [18]. The correlated truncation errors are obtained according to eq. 1 and eq. 2, and are shown as the brown lines at the  $1\sigma$  level. Uncorrelated uncertainties (blue band) underestimate the error in the pressure by as much as 30% near  $n_B = 2n_0$ , even though it agree with the correlated version on energy per particle within 10% (not shown here).

grid. It is not straightforward to translate this GP interpolated EOS on the uniform grid of  $k_F$  to another GP representation on a grid of different thermodynamic variables, as the physical inter-density correlations are not preserved in the process. This is a limitation due to GP where the kernels are translational invariant. Here, choosing either  $k_F$  or  $n_n$  is fine since the correlations captured by the basis functions are invariant under change of variables. Interpolation by polynomials does introduce systematics, though a simple estimate by dropping half the points and reproducing them using the remaining data points seems to indicate they are controlled and no more than  $\approx 5\%$ .

This prescription works well for both PNM and SNM EOSs, but the approach focuses on the PNM calculation from [17, 18]. The EOS for nuclear matter in beta-equilibrium is then constructed based on an expansion in proton fraction  $x_p = n_p/n_B$  described in [35]. This approach incorporates nuclear saturation properties by imposing a boundary condition at  $x_p = 1/2$ . Unlike those based on the parabolic expansion centered around  $x_p = 1/2$ , the resulting beta-equilibrium EOS is only moderately sensitive to the properties of SNM. While theoretical and experimental probes of SNM near and below saturation densities are very valuable inputs, they may suffer from currently unknown systematic uncertainties, as the recent neutron skin measurements might have indicated [36, 37]. Adding that neutron stars are mostly neutrons, this informed yet flexible approach is a noteworthy alternative to those in the literature for connecting nuclear physics to neutron star observables. For the

purpose of this work, the results are insensitive to the choices between SNM-centered or PNM-centered expansions, and only results based on the latter will be presented. A systematic comparison of the two and careful examinations of low-energy nuclear inputs will be reported in another work focusing on low-density EOSs.

## B. inner core EOS

At higher densities above  $n_{\chi\text{EFT}} \simeq 1 - 2n_0$  two approaches to describe the NS inner core are adopted. Firstly, I employ the limiting EOSs that have been long known in the literature. Their predictions in the mass-radius plane encircle all physical possibilities as they yield lower and upper bounds on the pressure at given densities. Due to their ability to delimit the physical regions in the EOS space, they lie at the center of the model-independent framework that propagates the information of cold quark matter at ultra-high densities down below. They will be discussed in detail in section IV. By examining how pQCD calculations impact these extreme scenarios I demonstrate that pQCD cannot improve bounds on NS static observables in section V.

In the second approach, I randomly generate inner core EOSs to explore how pQCD impacts the statistics of NS observables. Since pQCD does not change the boundaries in the mass-radius plane, their impacts on the probabilistic distributions (if and when relevant) would dependent upon the assumed NS models. Carefully examining the underlying assumptions in the EOS parameterizations is thus important to ensure robust constraints. I employ a family of speed of sound parameterizations detailed in [33]. Several subsets have been reported elsewhere in e.g. [38–40]. I have checked that the results below are robust against different choices of priors on EOS parameters (implicit or explicit), and across different subsets of inner core parameterizations.

## III. PERTURBATIVE QCD

At asymptotic densities, QCD becomes perturbative and renders useful an expansion in the strong coupling  $\alpha_s$ . The calculation of cold quark matter EOS up to N2LO is first performed in [19, 20] in the momentum space subtraction renormalization scheme, and remains the state-of-art full order calculation. Subsequent works formulated it in the widely adopted  $\overline{\text{MS}}$  scheme [22, 41], in which the pressure of unpaired quark matter with  $N_f = 3$  massless flavors is given by

$$P = N_f \frac{(\mu_B/3)^4}{4\pi^2} \left\{ 1 - \frac{2}{\pi} \alpha_s - \frac{N_f}{\pi^2} \alpha_s^2 \log \alpha_s - \frac{\alpha_s^2}{\pi^2} \left[ c_1 + N_f \left( \log \frac{N_f}{\pi} - c_2 \right) + \left( 11 - \frac{2}{3} N_f \right) \log X \right] + \mathcal{O}(\alpha_s^3) \right\} \quad (3)$$

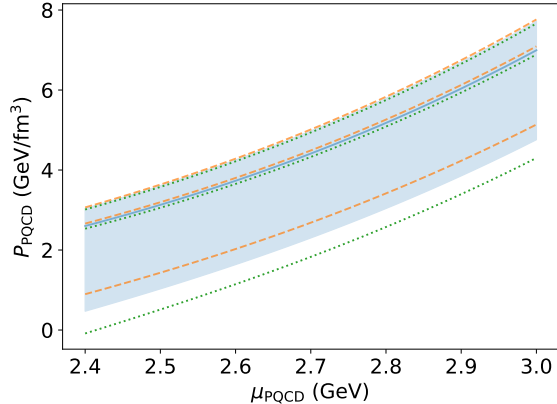


FIG. 2. The pQCD EOS up to N2LO. The blue band shows the renormalization scale uncertainties assuming  $\alpha_s(2 \text{ GeV}) = 0.2994$ , where the lower boundary corresponds to  $X = 1$ , the upper boundary corresponds to  $X = 4$ , and the blue solid line in between to  $X = 2$ . The green (orange) lines mark the same ranges for  $X = [1, 2, 4]$ , but assume the  $0.5\sigma$  upper (lower) bound of  $\alpha_s(2 \text{ GeV})$  (see appendix A).

Above,  $c_1 = 18 - 11 \log 2$  and  $c_2 = 0.535832\dots$  are numerical constants. The renormalization scale  $\bar{\Lambda}$  is implicit in  $\alpha_s \equiv \alpha_s(\bar{\Lambda})$  and is conveniently parameterized in terms of the baryon chemical potential by  $X = \bar{\Lambda}/(\mu_B/3)$ . Since the quark chemical potential  $\mu_q = \mu_B/3$  is the characteristic scale of the system, one might expect a good choice of the renormalization scale to be close to it ( $X \sim 1$ ). In ref [42] the authors compared predictions of eq. 3 to an exactly solvable large  $N_f$  limit where  $X$  is varied between  $1/2$  and  $2$ . It was found that the large  $N_f$  prediction lies somewhere in  $X \in [1, 2]$ , and is a bit closer to  $X = 2$ . Based on this observation, as well as empirical evidence from hot pQCD calculations, the dense quark matter community appears to have adopted fiducial values  $X = 1, 2, 4$  to estimate the renormalization scale uncertainties [22]. This range is shown in fig. 2 as the blue band.

Note that the appearance of  $X$  in eq. 3 is an artifact of the perturbation theory since physical observables shall be independent of it. Once higher order corrections are included, pQCD predictions are expected to show diminished sensitivity towards the renormalization scale, assuming pQCD is converging at given  $\mu_B$ . In this sense, the uncertainty associated with  $X$  is in fact a truncation error of the perturbation series. Efforts estimating the truncation error based on naturalness considerations are underway and will be reported in future work.

Another often neglected source of uncertainties comes from the running of  $\alpha_s$ . In the main text, the two-loop solution of  $\alpha_s$  consistent with eq. 3 is used. The uncertainty associated with the inferred value of  $\alpha_s$  can have a sizable impact on pQCD predictions. This is shown in fig. 2 as the dashed and dotted lines. The effect is especially prominent towards lower values of  $X$ , where

a percentage difference in the reference value  $\alpha_s(2 \text{ GeV})$  would shift the pressure on the order of  $20 - 50\%$ . Note that I do not claim the choice adopted here is the best. A few other options are discussed in appendix A. I merely wish to point out that the uncertainties associated with  $\alpha_s$  have to be properly accounted for before claiming robust constraints, and that extracting  $\alpha_s$  in the infrared is inherently challenging. For a recent review see [43].

Recently, partial N3LO contributions are computed in [23, 25, 44, 45] for the soft and mixed gluon sectors by resumming diagrams using EFT techniques [46–48]. The newly obtained contributions are the first two positive terms in the series, and hence predict higher pressure at given chemical potentials. However, if calculations of cold dense QED [49] or hot QCD [50, 51] were to be of any guide, the unknown hard contribution at N3LO is likely negative, and the net contribution at full order N3LO may drive the pressure even lower than that of eq. 3. In light of this, I take the cautious approach and employ the N2LO quark matter EOS in the main text. I comment on the impact of the soft contribution at N3LO and present the results in appendix B.

#### IV. THE LIMITING EOSs AND BOUNDS ON THE PRESSURE

In this section, I review the consistency requirement on low- and high-density EOSs at zero-temperature implied by the limiting scenarios well-known in the literature [29–32]. These extreme scenarios are simply consequences of causality and stability of dense matter, and are often colloquially referred to as the maximally stiff and maximally soft EOSs. They respectively yield the highest (lowest) and the lowest (highest) increments in pressure over arbitrary intervals in chemical potential (density). Since the baryon chemical potential  $\mu_B$  is the natural parameter in pQCD calculations, I will present these limiting EOSs in terms of  $\mu_B$  in a pedagogical approach.

In the  $\mu_B - P$  plane, the pressure  $P$  as a function of the baryon chemical potential  $\mu_B$  must be continuous and differentiable. Furthermore,  $P(\mu_B)$  is a convex function since

$$dP/d\mu_B = n_B, \quad (4)$$

$$\frac{d \log n_B}{d \log \mu_B} = C_s^{-1}, \quad 0 \leq C_s \leq 1. \quad (5)$$

where  $C_s$  is the speed of sound squared, a non-negative quantity for stable phases. Causality also imposes the additional requirement that  $C_s \leq 1$ . Together these relations suggest that for a given interval  $\Delta\mu_B = \mu_H - \mu_L$  between two arbitrary points labeled “L” and “H”, there exists an upper and a lower bound on  $\Delta P = P_H - P_L$ , where  $P_H = P(\mu_H)$  and  $P_L = P(\mu_L)$ .

To obtain the upper bound on  $\Delta P$ , the largest possible derivative  $\frac{dP}{d\mu_B} = n_B$  throughout the range  $[\mu_L, \mu_H]$  is desired. The schematics for the limiting cases of  $n_B(\mu_B)$

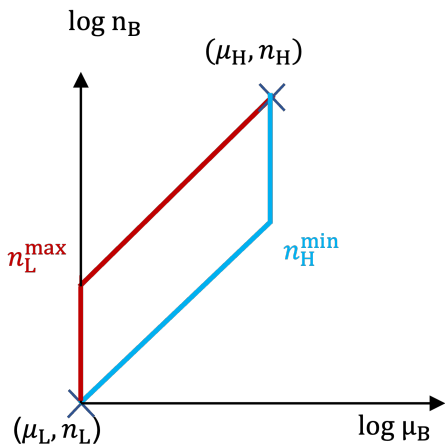


FIG. 3. The maximally stiff (blue) and maximally soft (red) EOSs between  $\mu_L$  and  $\mu_H$  that yield  $\Delta P_{\min}$  and  $\Delta P_{\max}$ .

is shown in fig. 3. At  $\mu_L$ , in order to get the largest value of the number density, one may introduce a first order phase transition which can raise  $n_B$  by an arbitrary amount at the expense of zero increase in  $\mu_B$ . But since the slope in the  $\log n_B - \log \mu_B$  plane is the inverse of the speed of sound squared, which must be no less than 1 as demanded by causality, jumps in the number density that are too large would overshoot  $n_H$  at  $\mu_H$ . To find the maximum of this value of  $n_L$ , one may start from  $(\mu_H, n_H)$  and follow the line with the least possible slope  $C_s^{-1} = 1$  down to  $\mu_L$ , where it gives

$$n_L^{\max} = n_H \exp \left[ \int_{\log \mu_H}^{\log \mu_L} d \log \mu_B \right] = n_H \frac{\mu_L}{\mu_H}. \quad (6)$$

This point is labeled in red in fig. 3. From there, the EOS I just followed from  $n_H$  downwards is the only allowed path to reach  $(\mu_H, n_H)$  without violating causality  $C_s \leq 1$ . In fact, this EOS predicts the largest possible number densities between  $\mu_L$  and  $\mu_H$ . Therefore, this construction shown in red in fig. 3 leads to the largest possible  $\Delta P$  given by

$$\Delta P_{\max} = \frac{n_H}{\mu_H} \int_{\mu_L}^{\mu_H} d\mu_B \mu_B = \frac{n_H \mu_H}{2} \left[ 1 - \left( \frac{\mu_L}{\mu_H} \right)^2 \right].$$

Following similar arguments one finds that the EOS depicted in blue in fig. 3 bears the lowest number densities between  $\mu_L$  and  $\mu_H$ . It starts at  $\mu_L$  with a constant  $C_s = 1$  and reaches  $\mu_H$  with a number density

$$n_H^{\min} = n_L \exp \left[ \int_{\log \mu_L}^{\log \mu_H} d \log \mu_B \right] = n_L \frac{\mu_H}{\mu_L}, \quad (7)$$

then climbs to  $n_H$  via a first order phase transition. The resulting lower bound on  $\Delta P$  reads

$$\Delta P_{\min} = \frac{n_L}{\mu_L} \int_{\mu_L}^{\mu_H} d\mu_B \mu_B = \frac{n_L \mu_L}{2} \left[ \left( \frac{\mu_H}{\mu_L} \right)^2 - 1 \right].$$

The constructions shown in red and blue in fig. 3 that give  $\Delta P_{\max}$  and  $\Delta P_{\min}$  are commonly referred to as the maximally soft and maximally stiff EOSs in the literature [29–32]. When expressed in terms of number densities, which is useful for describing NS inner cores, they are specified by

$$C_s(n_B) = \begin{cases} 0, & n_B \leq n_L + \Delta n_{\text{PT}} \\ 1, & n_B > n_L + \Delta n_{\text{PT}} \end{cases} \quad \text{maximally soft,} \quad (8)$$

$$C_s(n_B) = \begin{cases} 1, & n_B \leq n_L + \Delta n_{\text{onset}} \\ 0, & n_B > n_L + \Delta n_{\text{onset}} \end{cases} \quad \text{maximally stiff.} \quad (9)$$

Above, the parameters  $\Delta n_{\text{onset}}$  and  $\Delta n_{\text{PT}}$  that control the location and strength of phase transitions (the segment with  $C_s = 0$ ) are determined by the EOS at the endpoints, and I have just computed them indirectly in eqs. 6 and 7. When the maximally stiff and soft constructions are used to bound NS masses and sizes, these parameters are fixed by the NS maximum mass, also known as the TOV limit  $M_{\text{TOV}}$  [52, 53]. For specified  $M_{\text{TOV}}$ , the maximally stiff (soft) construction leads to the largest (smallest) radii at any given  $M \leq M_{\text{TOV}}$ .

To understand how  $\Delta P_{\min}$  and  $\Delta P_{\max}$  impose consistency requirements on the low-density endpoint when the high-density EOS at  $H$  is known, I consider two opposite scenarios in which they separately obtain. For low-density EOSs that are soft, i.e., predict high values of  $P_L$  at given  $\mu_L$ , stiff EOSs in the region between  $\mu_L$  and  $\mu_H$  are needed to reach the given high-density point specified by  $(\mu_H, n_H, p_H)$ . If however the low-density EOS is way too soft such that  $\Delta P = P_H - P_L < \Delta P_{\min}$ , even the maximally stiff EOS between  $\mu_L$  and  $\mu_H$  would overshoot  $p_H$  at  $\mu_H$ , suggesting a lack of causal and stable connections between the endpoints. Likewise, in the opposite limit, if the low-density EOS is too stiff predicting pressures that are hopelessly low, even the maximally soft EOS in the region  $[\mu_L, \mu_H]$  (which yields  $\Delta P_{\max}$ ) is unable to bring the pressure to  $P_H$  at  $\mu_H$ . Thus, for a given-high density endpoint  $H$ ,  $\Delta P_{\min}$  and  $\Delta P_{\max}$  can in principle rule out low-density endpoints that are inconsistent with thermodynamics and requires

$$\Delta P_{\min} \leq \Delta P \equiv P_H - P_L \leq \Delta P_{\max}$$

without explicitly parameterizing the EOS over the range  $[\mu_L, \mu_H]$ .

Below, I will take the pQCD predictions at  $\mu_{\text{pQCD}} \equiv \mu_H \simeq 2.5-3$  GeV as the high-density boundary condition and study the implications of  $\Delta P_{\max}$  and  $\Delta P_{\min}$

$$\Delta P_{\max} = \frac{n_{\text{pQCD}} \mu_{\text{pQCD}}}{2} \left[ 1 - \left( \frac{\mu_L}{\mu_{\text{pQCD}}} \right)^2 \right], \quad (10)$$

$$\Delta P_{\min} = \frac{n_L \mu_L}{2} \left[ \left( \frac{\mu_{\text{pQCD}}}{\mu_L} \right)^2 - 1 \right], \quad (11)$$

on neutron stars. While in principle both eqs. 10 and 11 can incorporate perturbative information about the cold quark matter at  $n_B \simeq 30 - 50n_0$  to put limits on the NS EOS at lower densities, I shall demonstrate that only eq. 10 can be robustly considered as a constraint, given our current understanding of the zero-temperature QCD phase diagram.

## V. IMPLICATIONS FOR NEUTRON STARS

Because of the large separation in density scales between the perturbative regime where pQCD is applicable and the strongly-interacting phase relevant for the interior of neutron stars, it is conceivable that pQCD may only impact (if at all) rather extreme NS EOSs that predict high densities in NSs. I shall show that such speculations are largely correct given the existence of two-solar-mass pulsars, but will clarify the context and criterion for the notion of “closeness”. I will also point out a necessary condition underlying all NS EOSs that are “close enough” to pQCD for which the latter could be relevant. Since the central density of the most massive neutron star is the highest realized in nature thus closest to that of pQCD, I shall always attempt the matching of NS EOS to pQCD via eqs. 10 and 11 at this density to maximize the constraining potentials, though occasionally matching at lower densities will be carried out for clarification purposes. For clarity, I colloquially refer to the NS EOS at the center of maximum-mass stars as the TOV point.

Refs [26, 27] appear to be the first to report pQCD constraints on the NS EOS through eqs. 10 and 11. The authors chose a few benchmark values of  $n_L \simeq 4 - 8n_0$  as the low-density matching point. Ref [28] pointed out matching at the TOV point is a better choice since the segment above it is not directly probed by NSs. Below, I will highlight the need to choose the EOS-dependent  $n_{\text{TOV}}$  and  $\mu_{\text{TOV}}$ , the number density and baryon chemical potential at the center of maximum-mass stars, as the low-density matching point, because they correlate with NS observables especially  $M_{\text{TOV}}$ . Properly taking into account these correlations is crucial to minimize assumptions about the ultra-dense matter not realized in nature.

Astrophysical observations of NSs have already provide valuable insights into the EOS and need to be incorporated to describe realistic neutron stars. In the main text, I will only explicitly take into account the existence of two-solar-mass NSs [54–58], because (1) these measurements are accurate and robust as they exploit relatively clean systems and make minimal assumptions (2) their implied limits on  $M_{\text{TOV}}$  can be translated to bounds on the NS EOS and NS radii through the maximally stiff and maximally soft EOSs, e.g. [32, 59]. Since potential pQCD constraints on NSs via  $\Delta P_{\text{min}}$  and  $\Delta P_{\text{max}}$  directly act upon the EOS space, this second benefit allows us to obtain model-independent bounds on NS static observables from pQCD. Temporarily deferring astrophysical

inputs on the NS radius  $R$  and deformability  $\Lambda$  also enables one to isolate the impact of high-density inputs, which helps elucidate the extent and strength of possible constraints on NSs coming from pQCD. I will show in the main text that pQCD cannot appreciably affect NS global observables such as the radius and the tidal deformability before any astrophysical constraints on these observables are imposed, though it does have the potential of ruling out a considerable number of NS EOSs. In appendix C I demonstrate the results remain valid when astrophysical bounds on  $R$  and  $\Lambda$  are taken into account.

The implications of  $\Delta P_{\text{max}}$  and  $\Delta P_{\text{min}}$  will be discussed separately due to their distinct dependencies on the endpoints and different sensitivities towards non-perturbative effects. As mentioned in section II, I employ the  $\chi\text{EFT}$ -based EOS up to  $n_{\chi\text{EFT}} \simeq 1 - 2n_0$ , where it is switched to either (1) the maximally stiff and soft inner cores to obtain bounds on NS observables; or (2) randomly generated inner cores to examine the statistics.

### A. $\Delta P_{\text{min}}$ is not a bound on NSs (yet)

I begin by discussing the implications of  $\Delta P_{\text{min}}$ . For a given low-density matching point  $\mu_{\text{TOV}}$ ,  $n_{\text{TOV}}$ , and  $P_{\text{TOV}}$ , eq. 11 is solely a function of  $\mu_{\text{pQCD}}$ . It is thus convenient to propagate the information of the TOV point to higher densities by extending the EOS upward using  $\Delta P_{\text{min}}$ . I then compare the extrapolated pressure based on  $\Delta P_{\text{min}}$  to pQCD predictions at  $\mu_{\text{pQCD}}$  in the perturbative regime. This leads to a lower limit on  $P_{\text{pQCD}} \equiv P(\mu_{\text{pQCD}})$ , requiring that

$$P(\mu_{\text{pQCD}}) \geq P_{\text{TOV}} + \Delta P_{\text{min}}(\mu_{\text{pQCD}}). \quad (12)$$

As explained earlier, violations of eq. 12 would occur if  $P_{\text{TOV}}$  is too high at  $\mu_{\text{TOV}}$ , so that  $P_{\text{TOV}} + \Delta P_{\text{min}}$  overshoots  $P_{\text{pQCD}}$  at the high-density matching point.

This extension by  $\Delta P_{\text{min}}$  is shown in fig. 4 for the maximally stiff and maximally soft NS EOSs that follow the extremes of  $2\sigma$   $\chi\text{EFT}$  up to  $n_{\chi\text{EFT}} = n_0$  (solid black) and  $n_{\chi\text{EFT}} = 2n_0$  (dashed black). The maximally soft NS EOSs are obtained by demanding  $M_{\text{TOV}} = 2M_{\odot}$ , while for the maximally stiff cases I take  $\Delta n_{\text{onset}} \rightarrow \infty$  in eq. 9 (turn off phase transitions) which yield the highest possible  $M_{\text{TOV}}$  for given low-density EOS below  $n_{\chi\text{EFT}}$ . The maximally stiff NS EOSs predict the highest  $P_{\text{TOV}}$  and are near the bottom of fig. 4, whereas the maximally soft constructions lead to the opposite limit predicting  $P_{\text{TOV}} \gtrsim 10^3 \text{ MeV fm}^{-3}$ . All four EOSs are truncated at their respective TOV points marked by “x”, where  $\Delta P_{\text{min}}$  is added and the sum is shown in orange. Equation 12 demands the orange lines to lie below  $P_{\text{pQCD}}$  (shown in blue) in order that the underlying NS EOSs are consistent with chosen pQCD calculations. For pQCD EOS with  $X \gtrsim 2$ ,  $P_{\text{pQCD}}$  lie well above the orange curves  $P_{\text{TOV}} + \Delta P_{\text{min}}(\mu_{\text{pQCD}})$ , suggesting all of the limiting NS EOSs satisfy eq. 12. However, if  $X \lesssim 1.5$ , soft NS EOSs

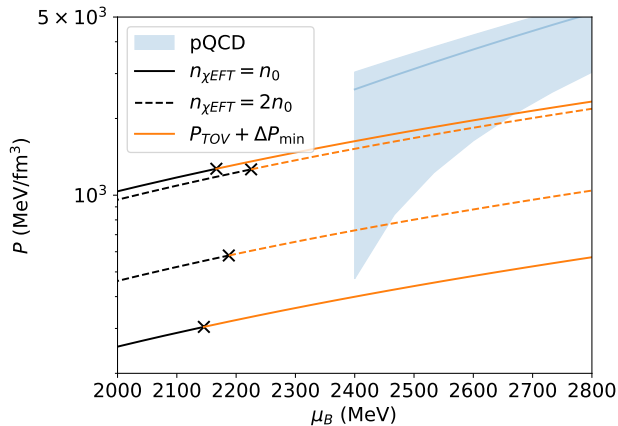


FIG. 4. The  $\Delta P_{\min}$  bound eq. 12 applied to the maximally stiff and soft NS EOSs. The blue band shows the range of pQCD predictions and is the same as in fig. 2. The solid (dashed) black lines show the limiting NS EOSs based on  $\chi$ EFT up to  $n_{\chi\text{EFT}} = 1.0n_0$  ( $2.0n_0$ ) then switched to the maximally stiff and soft inner cores. They both predict  $M_{\text{TOV}} \geq 2.0M_{\odot}$ , and are terminated at their respective TOV points marked by the black “x”. From there, they are extended by  $\Delta P_{\min}$  eq. 11 and yield the right-hand side of eq. 12. These extensions are shown in orange. By the  $\Delta P_{\min}$  bound eq. 12, any NS EOS whose orange extension lies above the blue curves are incompatible with the underlying pQCD EOS. For the four cases shown, while eq. 12 is always satisfied for pQCD with  $X \gtrsim 1.5$ , it is violated by those that predict very low  $P_{\text{pQCD}}$  ( $X \simeq 1$ ). However, this may not be viewed as a constraint on NS EOSs due to the unknown strengths of non-perturbative effect at  $\mu_{\text{pQCD}}$  not included here.

are in tension with pQCD and appear to be ruled out by eq. 12.

The obvious caveat is that  $P_{\text{pQCD}}$  currently has considerable uncertainties especially near lower values of  $X$  relevant for this constraint. Violations of eq. 12 only occur for pQCD EOSs with  $X \lesssim 1.3$ , or roughly  $P_{\text{pQCD}}(2.4\text{GeV}) \lesssim 1.3 \text{ GeV}/\text{fm}^3$ . The partial N3LO contribution raises  $P_{\text{pQCD}}$  and renders this constraint weaker, see fig. 15 in appendix B.

The central issue underlying the above argument is the assumption that the unpaired quark matter described by pQCD is the true ground state around  $\mu_{\text{pQCD}} \simeq 2.5 - 3 \text{ GeV}$ . Below  $\bar{\Lambda} \sim \mu_q \simeq \text{GeV}$  the strong coupling constant  $g_s = \sqrt{4\pi\alpha_s}$  that appears in the Lagrangian is above 1, suggesting non-perturbative effects could still dominate in this regime. Since the determination of ground state requires knowledge of all possible phases one is unable to make the call based on the pQCD EOS alone, even if its uncertainty can be significantly reduced.

In fact, the dense quark matter EOS is known to receive non-perturbative contributions from the pairing of quarks near their Fermi surface. Akin to Copper pairs in electric superconductors, this gives rise to color superconductivity [60–65] in the cold quark matter (CQM).

Assuming the ground state at  $\mu_B \gtrsim 2.5 \text{ GeV} \gg 3m_s$  is the most symmetric color-flavor-locked (CFL) superconducting phase, the pressure and density of the CQM are given by

$$\begin{aligned} P_{\text{CQM}} &= P_{\text{pQCD}} + P_{\text{CFL}}, \\ n_{\text{CQM}} &= n_{\text{pQCD}} + n_{\text{CFL}}, \end{aligned} \quad (13)$$

where

$$P_{\text{CFL}} = \frac{\Delta_{\text{CFL}}^2 \mu_B^2}{3\pi^2} \simeq 0.3 \text{ GeV}/\text{fm}^3 \left( \frac{\Delta_{\text{CFL}}}{100 \text{ MeV}} \right)^2 \left( \frac{\mu_B}{2.4 \text{ GeV}} \right)^2, \quad (14)$$

$n_{\text{CFL}} = \partial P_{\text{CFL}} / \partial \mu_B$ , and  $\Delta_{\text{CFL}}$  is the pairing gap which from the leading order  $\mathcal{O}(g_s)$  gap equation is given by  $\Delta_{\text{CFL}}/\mu_q \sim \exp(-\text{const}/g_s)$ . While estimates based on leading-order pQCD calculations suggest a modest gap  $\Delta_{\text{CFL}} \lesssim 10 - 50 \text{ MeV}$  [65], those rooted in phenomenological models reveal much larger possibilities  $\Delta_{\text{CFL}} \sim 50 - 200 \text{ MeV}$  at  $\mu_B \simeq 3 \text{ GeV}$  [64–69]. These values can vary by factors of a few in either direction depending on the color/flavor/spin structures of Cooper pairs, higher order corrections, and if non-standard pairings emerge [65].

Taking into account the pairing contribution, the  $\Delta P_{\min}$  bound eq. 12 should really read

$$P_{\text{pQCD}} + P_{\text{CFL}} \geq P_{\text{TOV}} + \Delta P_{\min}(\mu_{\text{pQCD}}). \quad (15)$$

It becomes apparent that the tension in fig. 4 is resolved if the deficit in  $P_{\text{pQCD}}$  is compensated by  $P_{\text{CFL}} \simeq 600 \text{ MeV fm}^{-3}$  at  $\mu_B = 2.4 \text{ GeV}$ , which translates to  $\Delta_{\text{CFL}} \simeq 200 \text{ MeV}$ . When the partial N3LO contribution is included, the deficit in pressure reduces and only requires  $\Delta_{\text{CFL}} \simeq 100 \text{ MeV}$ , see fig. 14.

The minimum pairing gap  $\min\{\Delta_{\text{CFL}}\}$  required to render *any* NS EOS that supports at least  $2M_{\odot}$  compatible with pQCD can be found by rearranging eq. 15, which leads to a lower bound on  $P_{\text{CFL}}$ :

$$\begin{aligned} P_{\text{CFL}}(\mu_B) &\geq P_{\text{TOV}} - P_{\text{pQCD}}(\mu_B) + \Delta P_{\min}(\mu_B) \\ &\equiv \Delta P(\mu_B) + \Delta P_{\min}(\mu_B). \end{aligned} \quad (16)$$

The right-hand side (RHS) of the above inequality has a global maximum across all NS inner core EOSs, and this maximum is reached by the maximally soft NS EOS eq. 8. I show this upper bound in fig. 5 as a function of the NS maximum mass. As noted earlier, violations of  $\Delta P_{\min}$  may only occur if  $X \lesssim 1.2$ , and with the partial N3LO contribution included the threshold tightens to  $X \lesssim 1.1$  (dashed line). For the N2LO pQCD EOS, gaps less than  $\simeq 200 \text{ MeV}$  are adequate to resolve *any* violations of eq. 12 given the existence of two-solar-mass pulsars, and with the N3LO term included,  $\Delta_{\text{CFL}} \lesssim 100 \text{ MeV}$  would suffice. It is for this reason I caution that  $\Delta P_{\min}$  shall not be considered as a bound on the NS EOS until the non-perturbative  $\Delta_{\text{CFL}}$  can be pinpointed exactly.

On the other hand, if higher order terms in pQCD narrow down  $P_{\text{pQCD}}(2.4 \text{ GeV})$  to be below  $\simeq 1.3 \text{ GeV}/\text{fm}^3$ ,

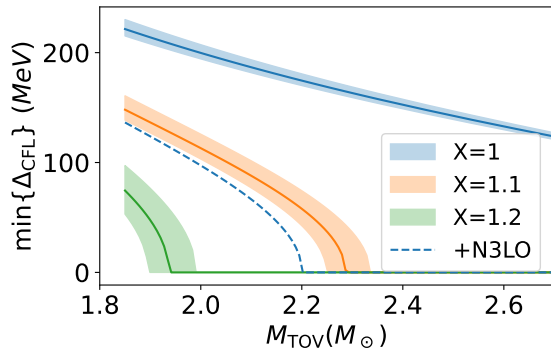


FIG. 5. Lowest superconducting gaps at  $\mu_B = 2.4$  GeV required to reconcile tensions with the  $\Delta P_{\min}$  bound for the maximally soft NS EOSs. These values are robust upper limits on the RHS of eq. 16, assuming  $\chi$ EFT is valid up to  $2n_0$ . That is to say, at given  $M_{\text{TOV}}$ , violations of the  $\Delta P_{\min}$  bound by *any* NS EOSs can be explained by pairing gaps no greater than the values shown here. The colors represent choices of the pQCD renormalization scale  $X$ , and the bands correspond to the  $2\sigma$   $\chi$ EFT uncertainties. The figure is cut off below  $M_{\text{TOV}} \leq 1.86M_{\odot}$ , the  $3\sigma$  lower limit of the inferred mass of PSR J0740+6620 [56, 58].

astrophysical evidence for a rather soft NS inner core EOS could indicate non-perturbative phenomena around  $\mu_B \simeq 2.4 - 3$  GeV. Assuming no additional repulsion is found in the cold quark matter, violations of the  $\Delta P_{\min}$  bound eq. 12 would strongly support a superconducting gap  $\Delta_{\text{CFL}} \simeq 50 - 200$  MeV *above* neutron star densities without directly probing it.

These at-best mild violations of the  $\Delta P_{\min}$  bound eq. 12 are due to the fact that  $P_{\text{TOV}}$  is bounded from above. This upper limit is given by the maximally soft NS inner core EOSs. The existence of  $2M_{\odot}$  pulsars robustly rules out softer EOSs that predict higher  $P_{\text{TOV}}$ , e.g., [32]. Had I not taken into account the two-solar-mass pulsars, much stronger violations of  $\Delta P_{\min}$  would have been allowed and consequently larger minimal superconducting gaps  $\min\{\Delta_{\text{CFL}}\}$  required to compensate these deficits. Our model-independent approach utilizing eq. 8 makes this fact explicit and robust. Furthermore, these results are insensitive to astrophysical uncertainties on  $M_{\text{TOV}}$ . Even if  $M_{\text{TOV}}$  is at the lower  $3\sigma$  inferred mass of PSR J0740+6620  $M \approx 1.87M_{\odot}$  [56, 58], the above discussion remains valid (see fig. 5).

### B. the $\Delta P_{\max}$ bound

For a chosen pQCD EOS at high-density matching point,  $\Delta P_{\max}$  eq. 10 only depends on  $\mu_L$ . It is therefore convenient to impose  $\Delta P_{\max}$  at the high-density endpoint and compare the resulting  $P_{\text{pQCD}} - \Delta P_{\max}$  with  $P_L$  at

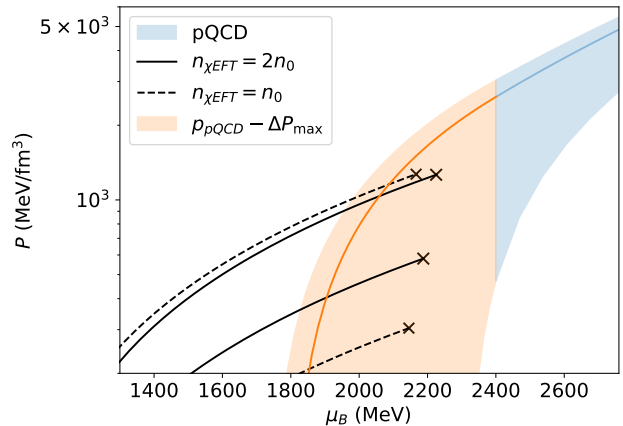


FIG. 6. The  $\Delta P_{\max}$  bound eq. 17 confronting the maximally stiff and maximally soft NS EOSs. The blue band shows the range of pQCD predictions up to N2LO, and is the same as in fig. 2. The solid (dashed) black lines depict NS EOSs following  $\chi$ EFT up to  $n_{\chi\text{EFT}} = n_0$  ( $2n_0$ ) then switched to the maximally stiff and soft inner cores. They are truncated at their respective TOV points, marked by the black “x”. The RHS of eq. 17 is shown in orange and is matched to pQCD at  $\mu_{\text{pQCD}} = 2.4$  GeV. The four limiting NS EOSs are only compatible with eq. 17 if  $X \lesssim 1.3$ . They are ruled out by a considerable region of the pQCD parameter space at  $\mu_{\text{pQCD}} = 2.4$  GeV. The brown stars labeled “critical point” mark the lowest densities at which the bound eq. 17 is violated. Although they lie quite deep inside the TOV points suggesting large sections of the EOSs are ruled out, these excluded segments are only concern stars very close to the TOV limit (see the red segments in fig. 8).

the low-density endpoint, requiring

$$P_L \geq P_{\text{pQCD}} - \Delta P_{\max}(\mu_L). \quad (17)$$

As in the previous subsection, I first consider the limiting NS inner core EOSs stitched at either  $n_{\chi\text{EFT}} = 2n_0$  (solid in fig. 6) or  $n_{\chi\text{EFT}} = n_0$  (dashed). They are shown in black in fig. 6 and are truncated at their respective TOV points. The RHS of eq. 17 is depicted in orange. The bound eq. 17 then rules out any NS EOS that lies above given orange curve, as it is incompatible with the assumed pQCD EOS upon which the  $\Delta P_{\max}$  extension under consideration is based. It is clear from fig. 6 that all four limiting NS EOSs are in tension with pQCD predictions at  $\mu_{\text{pQCD}} = 2.4$  GeV for  $X \gtrsim 1.6$ . This appears to be quite remarkable since the maximally soft EOSs predict the highest possible pressure  $P_{\text{TOV}}$ , and yet even these extreme values at around  $\mu_B \simeq 2.2$  GeV are still too low to reach the majority of pQCD EOSs at  $\mu_B = 2.4$  GeV. On the other end of the spectrum, predictions of  $P_{\text{TOV}}$  by the maximally stiff NS EOSs are the lowest possible and therefore in stronger tension with a wider range of pQCD calculations. However, owing to the untamed uncertainties associated with  $P_{\text{pQCD}}$ , even these extremely low values of  $P_{\text{TOV}}$  cannot be ruled out



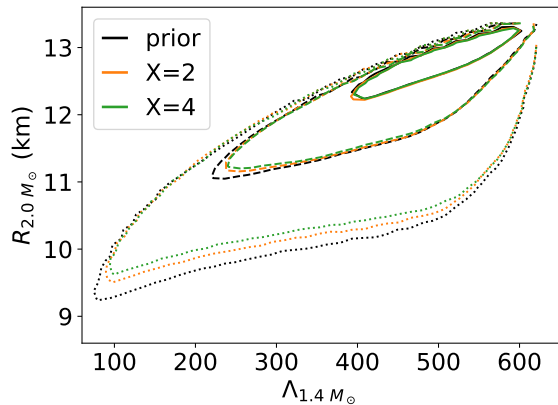


FIG. 7. Confidence intervals (CIs) on  $\Lambda_{1.4M_\odot}$  and  $R_{2.0M_\odot}$  before and after imposing the  $\Delta P_{\max}$  bound at  $\mu_{\text{pQCD}} = 2.4$  GeV assuming  $X = 2$  (orange) and  $X = 4$  (green). The solid, dashed, and dotted lines represent the 50%, 90%, and 99% CIs. The underlying EOS samples are generated following the  $\chi\text{EFT}$ -based low-density model up to  $n_{\chi\text{EFT}} = 2n_0$  and are described in section II. Only the existence of two-solar-mass NSs is imposed here. Using the N3LO  $\chi\text{EFT}$  EOS [18] up to  $n_{\chi\text{EFT}} = 2n_0$  automatically implies  $\Lambda_{1.4M_\odot} \lesssim 650$  (see also [32]). The posteriors are not appreciably different from the prior, suggesting the  $\Delta P_{\max}$  constraint is mostly orthogonal to current or expected astrophysical bounds.

completely as they are still compatible with eq. 17 when  $X \lesssim 1.3$ .

Since the maximally stiff and maximally soft inner cores delimit the space of all physical EOSs, it immediately follows that a wide range of NS EOSs may be at risk of being constrained by eq. 17. And for those that are in tension with pQCD, they cannot be ruled out completely because the maximally stiff NS EOSs are yet to be excluded robustly due to the large pQCD truncation errors manifested as a strong sensitivity towards  $X$ .

Figure 7 shows predictions for the radius of  $2M_\odot$  NSs and the tidal deformability of  $1.4M_\odot$  stars for about 10 million randomly generated samples following  $\chi\text{EFT}$  up to  $2n_0$ . Upon imposing eq. 17 between the EOS-dependent  $\mu_{\text{TOV}}$  and  $\mu_{\text{pQCD}} = 2.4$  GeV, about 20% of the samples in this pool are excluded<sup>1</sup>. I take  $X = 2$  and  $X = 4$  as they lead to the highest  $P_{\text{pQCD}}$  and consequently the most optimistic scenario for the  $\Delta P_{\max}$  constraint. This constraint neither affects appreciably the bounds on  $R_{2.0M_\odot}$  or  $\Lambda_{1.4M_\odot}$ , nor the correlations between the two observables. While there is a minor preference for slightly higher  $R_{2.0M_\odot}$  in the posterior, as the excluded samples tend to cluster around the lower end of

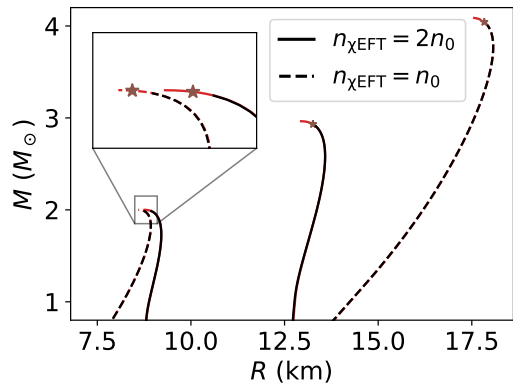


FIG. 8. Mass-radius relations for the maximally stiff and maximally soft NS EOSs. Only the segments shown in red are excluded by the  $\Delta P_{\max}$  bound imposed at  $\mu_B = 2.4$  GeV assuming  $X = 4$ . The rest of the curves depicted in black are compatible with the chosen pQCD EOS. The onsets of the red segments correspond to the critical points for the underlying NS EOSs, and those assuming  $X = 2$  are marked by brown stars as in fig. 6. In any case, no NSs further than  $\sim 0.06 M_\odot$  away from  $M_{\text{TOV}}$  are impacted by eq. 17.

$R_{2.0M_\odot}$  (because the central baryon chemical potentials at  $2M_\odot$  is further away from that at  $M_{\text{TOV}}$  for stiffer EOSs, see below), this shift is less than  $\approx 0.2$  km.

To understand better the feeble impacts on NS global observables by the  $\Delta P_{\max}$  bound eq. 17, let us explicitly examine the segments of NS EOSs affected by eq. 17. I begin by looking at the limiting scenarios shown in fig. 6. As explained earlier, violations of eq. 17 occur when an NS EOS crosses and lies above the chosen orange curve that is specific to a chosen pQCD renormalization scale  $X$ . Therefore, for any NS EOS that is in tension with eq. 17, only the segment above the crossing point is excluded. The low-density part preceding the crossing remains valid. The crossings will be referred to as the “critical” points.

In fig. 6 the critical points of the four limiting NS EOSs are marked by the brown stars assuming  $X = 2$ . Although significant portions of these EOSs lie above the critical point where the baryon chemical potential  $\mu_{\text{crit}} \simeq 1.8 - 2.0$  GeV, these high-density segments are only probed by stars very close to the maximum mass  $M_{\text{TOV}}$ . Excluded segments of the mass-radius curves are shown in red in fig. 8. For the maximally soft NS EOSs that support  $M_{\text{TOV}} = 2.0M_\odot$ , the lowest masses impacted by the aforementioned constraint are within  $0.01M_\odot$  to  $M_{\text{TOV}}$ . The maximally stiff NS EOSs are more susceptible to such constraints, yet only NSs heavier than about  $2.93M_\odot$  ( $4.04M_\odot$ ) for the one following  $\chi\text{EFT}$  up to  $n_{\chi\text{EFT}} = 2n_0$  ( $n_{\chi\text{EFT}} = n_0$ ) are affected. Considering their predictions for the maximum mass are  $M_{\text{TOV}} = 2.96M_\odot$  when  $n_{\chi\text{EFT}} = 2n_0$  and  $M_{\text{TOV}} = 4.09M_\odot$  when  $n_{\chi\text{EFT}} = n_0$ , it appears unlikely

<sup>1</sup> The fraction of samples excluded by pQCD constraints vary from  $\sim 10\%$  to  $\sim 60\%$  across different subsets of NS inner core parameterizations, but the effects on observables and EOSs are almost always insensitive to these choices.

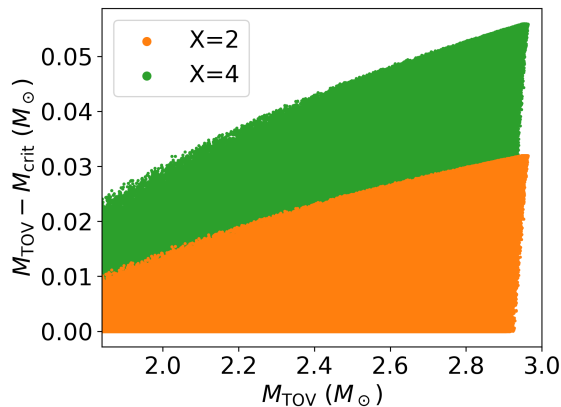


FIG. 9. The distance between  $M_{\text{crit}}$  and  $M_{\text{TOV}}$  for samples excluded by eq. 17 in fig. 7. They are also the minimal changes in  $M_{\text{TOV}}$  needed by the excluded NS EOSs to resolve their tension with eq. 17. These very short distance in NS masses  $M_{\text{TOV}} - M_{\text{crit}}$  between the critical point and the TOV point, combined with their considerable separations in baryon chemical potentials  $\mu_{\text{TOV}} - \mu_{\text{crit}}$  (see figs. 6 and 11), suggest that sufficiently flexible parameterizations of the NS EOS would not observe noticeable impacts on the size of NSs, since the EOS at TOV points (which eq. 17 directly constrains) would largely decouple from that at much lower  $\mu_B$  (which astrophysics probes).

that these minor effects may lead to detectable consequences. Below, for brevity, I shall refer to the lowest NS mass impacted by pQCD via eq. 17 as  $M_{\text{crit}}$ , i.e., the mass of the star whose central density is the critical point.

The radius of the star at the critical point  $R_{\text{crit}} \equiv R(M_{\text{crit}})$  is also very close to  $R_{\text{TOV}}$ . For the maximally soft NS EOS with  $n_{\chi\text{EFT}} = n_0$  ( $2n_0$ ),  $R_{\text{crit}}$  is about 0.1 km (0.1 km) larger than  $R_{\text{TOV}} = 8.6$  km (8.9 km), and for the maximally stiff EOS following  $\chi\text{EFT}$  up to  $n_0$  ( $2n_0$ ),  $R_{\text{crit}}$  is about 0.4 km (0.3 km) larger than  $R_{\text{TOV}} = 17.4$  km (12.9 km)<sup>2</sup>. This compounded with the nearly flat slopes  $dM/dR$  near the TOV limit strengthens the finding that pQCD is impotent in placing bounds on NS static observables.

Since all possibilities in the mass-radius plane are bracketed by predictions of the limiting NS EOSs<sup>3</sup>, it is safe to conclude in the absence of additional assumptions that eq. 17 only impacts stars in the vicinity of  $M_{\text{TOV}}$ . Figure 9 shows the proximity  $M_{\text{TOV}} - M_{\text{crit}}$  of critical masses to the TOV limits for excluded samples in fig. 7. For NS EOSs supporting higher  $M_{\text{TOV}}$ , pQCD constraints radiate further downwards but the effect is confined to a very limited range of NS masses throughout. Indeed, this is a ubiquitous feature shared by every

<sup>2</sup> Predictions of  $R_{\text{TOV}}$  by the maximally stiff NS EOSs are not a bound.

<sup>3</sup> except for dwarf neutron stars [70].

solutions to the TOV equation. For all the EOS samples considered, the derivatives of NS masses with respect to their central baryon chemical potential are small  $(dM/d\mu_c)_{2M_\odot} \lesssim 10^{-2} M_\odot/\text{MeV}$  for two-solar-mass stars and decreases rapidly at higher NS masses.

Our discussion above on the critical points hints at ways of modifying an excluded NS EOS to reconcile it with high-density inputs. Since the segment below  $\mu_{\text{crit}}$  already complies with eq. 17, the minimal modification would be to follow the original EOS up to the critical point, then stick to the  $\Delta P_{\text{max}}$  extension  $P(\mu_B) = P_{\text{pQCD}} - \Delta P_{\text{max}}(\mu_B)$  to avoid dropping below it. Implementations of this procedure entail a first order phase transition at  $\mu_{\text{crit}}$  (which gives rise to the sharp corner that bends the  $P(\mu)$  curve upwards), followed by a section of constant  $C_s = C_{s,\text{max}} = 1$ . Notice that this is exactly the scenario depicted in red in fig. 3, and the number density immediately after the phase transition is given by eq. 6. A simple estimate noting that  $n_{\text{pQCD}} \simeq 30 - 50n_0$  and  $\mu_{\text{crit}}/\mu_{\text{pQCD}} \gtrsim 0.5$  suggests the required jump in densities associated with the first order phase transition is typically huge ( $\Delta n_B \gtrsim 10n_0$ ,  $\Delta\mathcal{E} \gtrsim \text{GeV}/\text{fm}^3$ , see fig. 19 in appendix D), rendering stable NSs beyond the critical points infeasible. The outcome is an updated TOV limit that sits at  $M_{\text{TOV}}^{\text{new}} = M_{\text{crit}}$ .

I perform this modification for the excluded samples in fig. 7 and examine their updated predictions for astrophysical observables. As discussed earlier and shown in fig. 9, changes in the maximum mass  $\Delta M_{\text{TOV}} = M_{\text{TOV}} - M_{\text{crit}}$  and shifts in the radius of the maximum-mass stars  $\Delta R_{\text{TOV}} = R_{\text{TOV}} - R_{\text{crit}}$  are moderate at best. The relative differences  $\Delta M_{\text{TOV}}/M_{\text{TOV}}$  and  $\Delta R_{\text{TOV}}/R_{\text{TOV}}$  are both less than  $\approx 5\%$  for all the samples. Furthermore, neither the central value nor the probability distributions of  $R_{\text{TOV}}$  are appreciably affected, although those for  $M_{\text{TOV}}$  are shifted downwards moderately with  $\Delta M_{\text{TOV}} \lesssim 0.3M_\odot$ . This latter effect is prominent for samples predicting  $M_{\text{TOV}} \gtrsim 3M_\odot$  and can be somewhat sensitive to the priors. But in all scenarios the shift would not exceed  $\approx 0.5M_\odot$ . Therefore, even if the two-solar-mass pulsars observed so far turn out to be close to the actual TOV limit, pQCD considerations are still unable to affect the inference of their global properties appreciably. This is further confirmed by the probability distributions of both  $R_{\text{TOV}}$  and  $R_{2M_\odot}$  while demanding  $M_{\text{TOV}} < 2.3M_\odot$  [54–57], in the absence of this modification. For details see appendix C.

The modifications described above suggest that eq. 17 favors low sound speed near the TOV point. This preference is shown in fig. 10, where posteriors on the squared sound speed  $C_s$  are shifted downwards by the aforementioned pQCD constraint, an increasingly noticeable effect towards higher baryon chemical potentials. In appendix C I show that this shift is almost orthogonal to constraints expected from astrophysical observations.

It is striking that the pQCD constraint completely

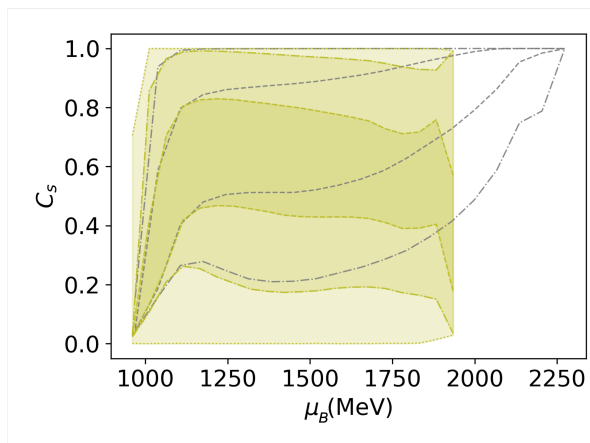


FIG. 10. The prior and posterior of the speed of sound squared  $C_s$  for the pQCD constraint in fig. 7. The yellow dashed, dash-dotted, and dotted lines are the 50%, 90%, and 100% posterior CIs respectively, whereas the gray lines show the 50% and 90% priors. The prior appears to be biased toward larger  $C_s$ , but this is a consequence of truncating each EOS at its TOV point, and only EOSs with larger  $C_s$  predict higher  $\mu_{\text{TOV}}$  (see fig. 11). That the prior is indeed flat is confirmed in fig. 16. This shift in the posterior CIs shown here appears to be the strongest effect eq. 17 could impart to the inference of NS EOSs.

rules out  $\mu_{\text{TOV}} \gtrsim 1.9$  GeV in the posterior in fig. 10. But this is not surprising considering that even the maximally soft NS EOSs, whose predictions for  $P_{\text{TOV}}$  are the highest, are excluded in fig. 6 if  $X \gtrsim 1.6$ . In other words, the bound eq. 17 demonstrates higher sensitivity toward  $\mu_{\text{TOV}}$  over  $P_{\text{TOV}}$ , in the sense that an NS EOS is more likely in tension with pQCD if it accommodates higher  $\mu_{\text{TOV}}$ , almost independent of its prediction for  $P_{\text{TOV}}$ , as compared with those predicting lower  $\mu_{\text{TOV}}$ . For example, when matched to pQCD at  $\mu_{\text{pQCD}} = 2.4$  GeV, all of the NS EOSs excluded by eq. 17 predict  $\mu_{\text{TOV}} \gtrsim 1.8$  GeV. These observations help establish a simple criterion on the applicability of eq. 17. I find that the maximum speed of sound squared  $C_{s,\text{max}}$  of an NS EOS informs  $\mu_{\text{TOV}}$ . Assuming  $\chi\text{EFT}$  is valid up to  $n_{\chi\text{EFT}} = n_0$  ( $2n_0$ ),  $C_{s,\text{max}}$  needs to exceed  $\approx 0.5$  ( $0.6$ ) in order that  $\mu_{\text{TOV}} \gtrsim 1.8$  GeV. This correlation also explains the seemingly biased sample selections shown in fig. 10: the prior on  $C_s$  favors higher  $C_s$  with increasing  $\mu_B$  because only EOSs with larger  $C_{s,\text{max}}$  would lead to higher  $\mu_{\text{TOV}}$ , and if the EOSs are not truncated at their respective TOV points the prior would be mostly flat and featureless. The CIs plotted against number densities shown in fig. 16 also corroborate this.

I show the correlation between  $C_{s,\text{max}}$  and  $\mu_{\text{TOV}}$  in fig. 11. For the strongest constraint with  $X = 4$  (green), eq. 17 becomes relevant starting at  $\mu_{\text{TOV}} \gtrsim 1.8$  GeV (see also fig. 6), and rules out all NS EOSs with  $\mu_{\text{TOV}} \gtrsim 1.9$  GeV. For given  $C_{s,\text{max}}$ , the maximally soft NS EOSs shown as the black curves give the upper bound on  $\mu_{\text{TOV}}$  where the bands correspond to the

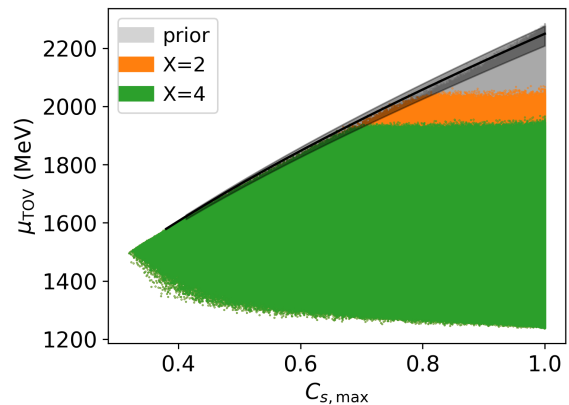


FIG. 11.  $C_{s,\text{max}} \gtrsim 0.6$  inside NSs is a necessary condition for NS EOSs constrained by the  $\Delta P_{\text{max}}$  consideration. The collection of EOS samples is shown in gray. The black curve is based on the maximally soft NS EOSs and yield the highest possible  $\mu_{\text{TOV}}$  at fixed  $C_{s,\text{max}}$ . Its surrounding bands reflect the  $\pm 2\sigma$   $\chi\text{EFT}$  uncertainties. Upon imposing the  $\Delta P_{\text{max}}$  bound at  $\mu_{\text{pQCD}} = 2.4$  GeV the posteriors for  $X = 2$  and  $X = 4$  are shown in orange and green respectively. All of the excluded samples predict  $\mu_{\text{TOV}} \gtrsim 1.8$  GeV, requiring  $C_{s,\text{max}} \gtrsim 0.6$  inside NSs.

$2\sigma$   $\chi\text{EFT}$  uncertainties. They reach  $\mu_{\text{TOV}} = 1.8$  GeV at around  $C_{s,\text{max}} = 0.6$  thus set a lower bound on  $C_{s,\text{max}}$  required for any EOS to be “close enough” to pQCD densities. The upshot is that an NS EOS cannot violate eq. 17 unless  $C_{s,\text{max}} \gtrsim 0.6$  inside NSs. This is only a necessary condition, and  $C_{s,\text{max}} \gtrsim 0.6$  does not automatically lead to the violation of eq. 17.

Up until now, I have focused on the most optimistic scenarios where the matching to pQCD is performed at  $\mu_{\text{pQCD}} = 2.4$  GeV, and have chosen  $X = 4$  which yields the highest pressure  $P_{\text{pQCD}}$ . The constraints weaken drastically if the matching point is raised to higher baryon chemical potentials. For eq. 17 imposed at  $\mu_{\text{pQCD}} = 2.6$  GeV, only NS EOSs with  $C_{s,\text{max}} \gtrsim 0.75$  can potentially be ruled out, a condition tightens to  $C_{s,\text{max}} \gtrsim 0.9$  for matching at  $\mu_{\text{pQCD}} = 2.8$  GeV. If pQCD is imposed above  $\mu_B \approx 2.9$  GeV, eq. 17 becomes completely irrelevant. Furthermore, lowering the renormalization scale  $X$  also reduces the strength of such constraints. At  $X = 1$ , no NS EOSs that support  $2M_{\odot}$  can be ruled out, even with soft N3LO contribution to the dense quark matter EOS included.

To account for the pQCD truncation error manifested as dependencies on  $X$ , I perform a simple inference by noting that while uncertainties associated with  $P_{\text{pQCD}}$  are huge, those of the number densities are controlled. I therefore fix  $n_{\text{pQCD}}$  to the fiducial value  $n_B = 5 \text{ fm}^{-3}$ , but sample  $P_{\text{pQCD}}$  randomly from a uniform (and log-uniform) distribution on  $[0.5, 3] \text{ GeV}/\text{fm}^3$ , the approximate range of pQCD predictions at  $\mu_{\text{pQCD}} = 2.4$  GeV

with  $X \in [1, 4]$ . Analysis in fig. 10 is then repeated but with this mocked  $P_{\text{pQCD}}$  data instead. Unsurprisingly, the posteriors on  $C_s$  are almost identical to the priors even for  $\mu_B \gtrsim 2.0$  GeV, a result independent of values of  $\mu_{\text{pQCD}}$ , whether varying  $n_{\text{pQCD}}$ , or if the N3LO contributions are included (appendix B)<sup>4</sup>. Since the constraints on  $C_s(\mu_B)$  appear to be the strongest, and incorporating uncertainties associated with the running of  $\alpha_s$  will further broaden error bands (see appendix A), it appears that meaningful and robust constraints on the NS EOS from pQCD is infeasible at the moment.

I conclude with cautious optimism by providing a forecast on the presumption that  $P_{\text{pQCD}}$  at  $\mu_B = 2.4$  GeV will be reliably and accurately determined. For  $P_{\text{pQCD}}(2.4 \text{ GeV}) = 3 \text{ GeV}/\text{fm}^3$ , the median value of the squared sound speed at the center of maximum-mass stars,  $C_{s,\text{TOV}}$ , is expected to be lowered by up to 0.2-0.3 by eq. 17, whereas for  $P_{\text{pQCD}}(2.4 \text{ GeV}) = 2 \text{ GeV}/\text{fm}^3$  the anticipated effect drops to about 0.1-0.2, and would be less than  $\sim 0.05$  if  $P_{\text{pQCD}}(2.4 \text{ GeV}) = 1.5 \text{ GeV}/\text{fm}^3$  hardly distinguishable from systematic uncertainties due to assumptions in the underlying NS EOSs. Again, these forecasted bounds are almost orthogonal to expected astrophysical constraints, unless highly specific features are assumed for NS EOSs.

### C. eq. 17 is the necessary and sufficient condition

As noted above, compliance with eq. 17 at  $\mu_L = \mu_{\text{TOV}}$  is the sufficient condition for a given NS EOS, and ensuring it holds for all  $\mu_L < \mu_{\text{TOV}}$  is the necessary condition. Hence from a practical point of view, one only needs to check eq. 17 at the TOV point of each NS EOS to determine if the constraint applies. Discussions on the critical point  $\mu_{\text{crit}} < \mu_{\text{TOV}}$  only serve to clarify the constraining power of pQCD, and are not necessary in general.

Recently, a so-called integral constraint is proposed in ref [26]. It is formulated in the  $\mu_B - n_B$  plane and is a weaker version of the necessary condition discussed above, see appendix D. Note that the way it has been applied is only approximate as the (comparatively controlled and less important for the current purpose) uncertainties associated with  $\chi\text{EFT}$  are ignored. Even though this constraint on number density does not reveal additional information beyond what is encoded in eq. 17, it helps visualize the phase transitions required to reconcile tensions with the  $\Delta P_{\text{max}}$  bound, and enables constraints on the pressure-energy density relation [26].

<sup>4</sup> Priors favoring large  $P_{\text{pQCD}}$  would help, though it is not clear if such choices are justified. I impose priors on  $P_{\text{pQCD}}$  as it is directly involved in the  $\Delta P_{\text{max}}$  bound. Choosing instead priors on  $X$  is also valid but obscures this connection, and the resulting shape of the distribution on  $P_{\text{pQCD}}$  might not be invariant once higher order terms in pQCD are known.

## VI. DISCUSSION AND CONCLUSION

Aided by the model-independent bounds on the EOS [29–32, 59], I have shown that ab-initio cold quark matter calculations in the perturbative regime have the potential of placing robust bounds on the EOS if NSs probe baryon chemical potentials greater than about  $\mu_B \sim 1.8 - 2.0$  GeV. The higher the baryon chemical potential realized, the tighter the constraint becomes. If the pressure of NS EOS is too high, the absence of a valid construction between  $\mu_{\text{TOV}}$  and  $\mu_{\text{pQCD}}$  may indicate the presence of non-perturbative effects near  $\mu_B \lesssim 3$  GeV. Until the pairing gap can be reliably and accurately calculated, such consideration may not be viewed as a robust constraint on the NS EOS.

On the other hand, an NS EOS may be incompatible with high-density inputs if its prediction for the pressure is too low to reach  $P_{\text{pQCD}}$ . This is embodied in the  $\Delta P_{\text{max}}$  bound eq. 17, and is the sole requirement an NS EOS needs to comply with currently. Constraints of this type only concern the high-density tails of NS EOSs relevant for stars very close to their respective TOV limits ( $M_{\text{TOV}} - M_{\text{crit}}$  no more than  $0.06M_{\odot}$  for  $M_{\text{TOV}} = 4M_{\odot}$ , a bound decreases with decreasing  $M_{\text{TOV}}$ ), therefore cannot directly affect observables for most NSs. The strongest constraint possible (at  $\mu_{\text{pQCD}} = 2.4$  GeV, assuming  $X = 4$  and including the N3LO soft contributions that push  $P_{\text{pQCD}}$  higher) can at best rule out  $R_{\text{TOV}} \lesssim 9.5$  km, or compactness of the maximum-mass stars  $C_{\text{TOV}} = M_{\text{TOV}}/R_{\text{TOV}} \gtrsim 0.33$ , assuming  $\chi\text{EFT}$  is valid up to  $n_0$ . Even if the two-solar-mass pulsars observed to date are in fact the TOV limit, such constraints would only raise the median value of  $R_{2M_{\odot}}$  by no more than 0.2 km. Accounting for the uncertainties of pQCD requires choosing a prior on the renormalization scale  $X$ . With natural choices of priors no meaningful bounds can be derived at the moment owing to the wild uncertainties associated with  $P_{\text{pQCD}}$ .

Although the bound eq. 17 directly applies to the pressure, it is more sensitive to predictions of  $\mu_{\text{TOV}}$  by NS EOSs, as even the highest  $P_{\text{TOV}}$  by the maximally soft NS EOS at  $\mu_{\text{TOV}} \gtrsim 2$  GeV is too low to reach  $P_{\text{pQCD}}$  for  $X \gtrsim 2$  (see fig. 6). Any NS EOS predicting  $\mu_{\text{TOV}} \gtrsim 1.8$  GeV is at risk of being ruled out by such considerations. The necessary condition for supporting high values of  $\mu_{\text{TOV}}$  is large  $C_{s,\text{max}} \gtrsim 0.6$  inside NSs, see fig. 11.

Unlike the scenarios in section V A, the  $\Delta P_{\text{max}}$  bound in section V B is insensitive to non-perturbative effects. This is because eq. 17 only obtains for high pressure in the quark matter  $P_{\text{pQCD}} \gtrsim 2 \text{ GeV}/\text{fm}^3$  where contributions from a typical pairing gap  $\Delta \simeq 200$  MeV  $P_{\text{CFL}}/P_{\text{pQCD}} \sim (\Delta_{\text{CFL}}/\mu_q)^2$  would be moderate at best, whereas in section V A only pQCD calculations predicting low pressure are relevant. The  $\Delta P_{\text{max}}$  constraint also appears to be insensitive to the strange quark mass  $m_s$ . In the decoupling limit  $m_s \rightarrow \infty$ , the 2-flavor quark matter EOS only differs by about 20% at  $\mu_B = 2.6$  GeV, moving the bands in fig. 10 by no more than  $\approx 10\%$ .

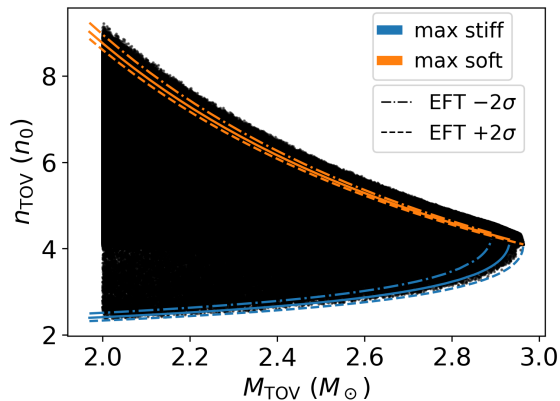


FIG. 12. Correlations between  $n_{\text{TOV}}$  and  $M_{\text{TOV}}$ . Stiff NS EOSs supporting high  $M_{\text{TOV}}$  tend to probe lower densities than those reached by their soft counterparts. The lower bounds are given by the maximally stiff NS EOSs shown in blue. Assuming twin stars are absent, the maximally soft NS EOS shown in orange roughly delimit the upper boundary. The dashed lines indicate the  $2\sigma$   $\chi$ EFT uncertainties.

Recently, ref [26] reported another *necessary* condition. As discussed above and detailed in appendix D, this necessary condition does not lead to additional constraints beyond eq. 17. By matching NS EOSs at a fixed density  $n_B \simeq 5 - 10n_0$ , that letter and the following work [27] excluded a large number of EOSs based on their segments that are not probed by stable NSs. This is especially problematic for stiff NS EOSs as their predictions for  $n_{\text{TOV}}$  are typically low but for  $P(n_B \simeq 5 - 10n_0 > n_{\text{TOV}})$  are high. To illustrate this point the correlation between  $M_{\text{TOV}}$  and  $n_{\text{TOV}}$  is shown in fig. 12. The boundaries in this figure can be reproduced by the maximally stiff (blue) and maximally soft NS EOSs (orange). Failing to account for these correlations would unfairly bias against large values of  $M_{\text{TOV}}$ . Ref [28] correctly addressed this issue, but arrived at the misleading conclusion that pQCD is not constraining if imposed on top of current astrophysical observations. It has been clarified that eq. 17 is only relevant for stars very close to the TOV limit so would not affect neutron star observables appreciably, but could yield constraints on the EOS that are mostly orthogonal to astrophysical bounds. Additionally, their claim regarding the possible interplay between pQCD constraints and  $R_{2.0M_\odot} \gtrsim 13$  km is likely due to implicit biases in the parameterization of inner core EOSs, which is an approximation to a subset of the ensembles employed in this work. For flexible parameterizations the EOS at the TOV point would largely decouple from that at lower densities, see figs. 6, 8 and 9. Addressing implicit assumptions in the parameterizations of NS EOSs is important and is relevant for a wider range of issues but requires a much much lengthier discussion and will be reported in separate work [71]. Finally, we reiterate that eq. 12 may not be viewed as a constraint on NSs

yet as it is sensitive to the undetermined strength of the superconducting gap. Given the existence of two-solar-mass pulsars, moderate pairing gaps  $\Delta_{\text{CFL}} \lesssim 200$  MeV consistent with current estimates are sufficient to explain any possible violations.

Reducing the uncertainties of the cold quark matter EOS is crucial in materializing the potentials demonstrated in section V B. As noted earlier, although typically referred to as the renormalization scale uncertainties, it is a form of truncation error in disguise, as the dependency on  $X$  is an artifact that is expected to receive cancellations when higher order terms are known. This is shown to be the case in dense QED [49] and hot QCD calculations [50, 51]. One would expect it to hold in dense QCD as well assuming pQCD is a valid description down to  $\mu_q \simeq \text{GeV}$ . The recently obtained leading and next-to-leading soft contributions resummed to all orders appear to support the convergence [72]. Effort employing strategies developed in  $\chi$ EFT [34] to understand better pQCD truncation errors is underway and will be reported in future work.

This work largely confirms previous findings that the knowledge of neutron star global properties alone may not be adequate to distinguish the relevant microscopic degrees of freedom inside the cores of NSs [73]. Although pQCD EOSs predicting high pressure can place upper bounds on the speed of sound above  $\mu_B \gtrsim 2$  GeV, I caution against interpreting this as evidence for quark matter, as extrapolating  $C_s$  from pQCD predictions above  $\mu_B \sim 2.5$  GeV to the strongly-interacting phase at such low densities may be unwarranted. Understanding the phase of matter in this intermediate density range is inherently challenging as neither pQCD nor NSs directly probe this regime. The ensuing letters in this series aim to fill this gap and report model-independent studies on the ultra-dense matter.

Very recently, ref [74] performed a Bayesian analysis based on parameterizing the NS EOS to infer upper bounds on the superconducting gap. I wish to point out that this constraint can be obtained model-independently with the help of maximally soft NS EOSs, see appendix E.

## ACKNOWLEDGMENT

I would like to thank Sanjay Reddy for discussions. During the conception and completion of this work the author is supported by Grant No. PHY-1430152 (JINA Center for the Evolution of the Elements) and the Institute for Nuclear Theory Grant No. DE-FG02-00ER41132 from the Department of Energy, and by NSF PFC 2020275 (Network for Neutrinos, Nuclear Astrophysics, and Symmetries (N3AS)).

### Appendix A: the running of $\alpha_s$

This appendix is a brief overview of the uncertainties associated with  $\alpha_s \equiv g_s^2/(4\pi)^2$  around GeV scales. To obtain the strong coupling constant at a given scale  $\bar{\Lambda}$  I solve the renormalization group equation

$$\frac{d\alpha_s}{d \log \bar{\Lambda}^2} = - \sum_{i \geq 0} \frac{\beta_i}{(4\pi)^{i+1}} \alpha_s^{i+2} = - \sum_{i \geq 0} b_i \alpha_s^{i+2} \quad (\text{A1})$$

$$\beta_0 = 11 - \frac{2N_f}{3}, \quad (\text{A2})$$

$$\beta_1 = 102 - \frac{38N_f}{3}, \quad (\text{A3})$$

$$\beta_2 = \frac{325N_f^2}{54} - \frac{5033N_f}{18} + \frac{2857}{2}, \quad (\text{A4})$$

$$\beta_3 = \frac{149753}{6} + 3564\zeta_3 - \left( \frac{1078361}{162} + \frac{6508}{27}\zeta_3 \right) N_f + \left( \frac{50065}{162} + \frac{6472}{81}\zeta_3 \right) N_f^2 + \frac{1093}{729} N_f^3, \quad (\text{A5})$$

$$\begin{aligned} \beta_4 = & \frac{8157455}{16} + \frac{621885}{2}\zeta_3 - \frac{88209}{2}\zeta_4 - 288090\zeta_5 + \left( -\frac{336460813}{1944} - \frac{4811164}{81}\zeta_3 + \frac{33935}{6}\zeta_4 + \frac{1358995}{27}\zeta_5 \right) N_f \\ & + \left( \frac{25960913}{1944} + \frac{98531}{81}\zeta_3 - \frac{10526}{9}\zeta_4 - \frac{381760}{81}\zeta_5 \right) N_f^2 \\ & + \left( -\frac{630559}{5832} - \frac{48722}{243}\zeta_3 + \frac{1618}{27}\zeta_4 + \frac{460}{9}\zeta_5 \right) N_f^3 + \left( \frac{1205}{2916} - \frac{152}{81}\zeta_3 \right) N_f^4, \end{aligned} \quad (\text{A6})$$

where  $\zeta_n \equiv \zeta(n)$  are values of the Riemann zeta function. Coefficients beyond 2 loop ( $\beta_1$ ) are renormalization scheme dependent, and the values quoted above are given in  $\overline{\text{MS}}$ . Equation A1 can be solved either numerically, or analytically albeit approximately in a perturbative fash-

up to 2, 3, 4 and 5 loops. For  $N_c = 3$  QCD with  $N_f$  active flavors of quarks the beta function coefficients are given by [75]

ion. Defining  $t = 2 \log(\bar{\Lambda}/\bar{\Lambda}_{\overline{\text{MS}}})$  and  $l = \log(t)$ , an iterative solution to the 5-loop renormalization group equation ( $\mathcal{O}(\alpha_s^6)$  on the right hand side of eq. A1) is given by

$$\alpha_s(\bar{\Lambda}^2) = \frac{1}{b_0 t} \left[ 1 - \frac{b_1 l}{b_0^2 t} + \frac{b_1^2 (l^2 - l - 1) + b_0 b_2}{b_0^4 t^2} + \frac{b_1^3 (-2l^3 + 5l^2 + 4l - 1) - 6b_0 b_1 b_2 l + b_0^2 b_3}{2b_0^6 t^3} \right. \\ \left. + \frac{18b_0 b_2 b_1^2 (2l^2 - l - 1) + b_1^4 (6l^4 - 26l^3 - 9l^2 + 24l + 7) + 2b_0^2 (5b_2^2 + b_0 b_4) - b_0^2 b_1 b_3 (12l + 1)}{6b_0^8 t^4} \right]. \quad (\text{A7})$$

Its exact derivatives up to the second order are

$$\begin{aligned} \frac{d\alpha_s(\bar{\Lambda}^2)}{d \log \bar{\Lambda}^2} = & -\frac{1}{b_0 t^2} \left[ 1 + \frac{b_1(1-2l)}{b_0^2 t} + \frac{b_1^2(-2-5l+3l^2) + 3b_0 b_2}{b_0^4 t^2} \right. \\ & + \frac{b_1^3(-4+3l+13l^2-4l^3) + 3b_0 b_2 b_1(1-4l) + 2b_0^2 b_3}{b_0^6 t^3} \\ & \left. + \frac{b_1^4(11+138l+33l^2-154l^3+30l^4) + 18b_0 b_2 b_1^2(-4-9l+10l^2) + b_0^2 b_3 b_1(7-60l) + 10b_0^2(5b_2^2 + b_0 b_4)}{6b_0^8 t^4} \right], \end{aligned} \quad (\text{A8})$$

$$\frac{d^2\alpha_s(\bar{\Lambda}^2)}{d(\log \bar{\Lambda}^2)^2} = \frac{2}{b_0 t^3} \left[ 1 + \frac{b_1(5-6l)}{2b_0^2 t} + \frac{b_1^2(-3-26l+12l^2) + 12b_0 b_2}{2b_0^4 t^2} + \frac{-b_1^3(23+11l-77l^2+20l^3) + 3b_0 b_2 b_1(9-20l) + 10b_0^2 b_3}{2b_0^6 t^3} + \frac{3b_0 b_2 b_1^2(60l^2-74l-15) + b_1^4(127l+110l^2-174l^3+30l^4) + b_0^2 b_3 b_1(17-60l) + 10b_0^2(5b_2^2 + b_0 b_4)}{2b_0^8 t^4} \right]. \quad (\text{A9})$$

I do not use the renormalization group equation eq. A1 to compute the derivatives as eq. A7 is only an approximate solution to the 5-loop renormalization group equation. The residue, although small, would spoil the thermodynamic consistency of the pQCD EOS if eq. A1 were to be used in calculating  $n_B = \frac{dP}{d\mu_B}$  and  $C_s = d \log \mu_B / d \log n_B$ .

The 2-, 3-, 4-loop solutions of  $\alpha_s$  can be obtained by setting  $b_{i>n_{\text{loop}}-1} = 0$  where  $n_{\text{loop}} = 2, 3, 4$ . It is also customary, although not necessary, to truncate the iterative solutions in eq. A7 at order  $\left(\frac{b_i}{b_0^2}\right)^{n_{\text{loop}}-1}$  in the literature, i.e., only keep the leading power in  $b_{n_{\text{loop}}-1}$ . This convention is adopted throughout the manuscript.

The Landau pole  $\bar{\Lambda}_{\overline{\text{MS}}}$  is determined once the strong coupling at a given reference scale is specified. Above, I took the value  $\alpha_s(\bar{\Lambda} = 2 \text{ GeV}) = 0.2994_{-0.0141}^{+0.0152}$  from the 2008 particle data group (PDG) report. The resulting  $P_{\text{pQCD}}$  and its uncertainties at  $\mu_B = 2.4 \text{ GeV}$  are shown in fig. 13. Since then, PDG only reports  $\alpha_s(\bar{\Lambda} = M_Z)$ . Running  $\alpha_s$  from the Z boson mass  $M_Z \sim 100 \text{ GeV}$  to GeV scales is not straightforward as the decoupling of both charm and bottom quarks occurs in this regime. But because the uncertainties of  $\alpha_s(M_Z)$  are barely reduced since 2008, one would not expect significant improvements for the bound on  $\alpha_s(2 \text{ GeV})$  quoted above. Furthermore, the current inferred values of  $\alpha_s(M_Z)$  could suffer from non-negligible modeling uncertainties as a few subsets of measurements behind the PDG averaged value appear to be in disagreement [76]. A careful running of  $\alpha_s$  from  $M_Z$  where  $N_f = 5$  to GeV scales where  $N_f = 3$  will be performed in a future work.

An alternative approach is to take the values of Landau pole  $\bar{\Lambda}_{\overline{\text{MS}}}$  reported in the literature. This is generally disfavored as these values can be quite sensitive to the order of renormalization group equations used in the analysis. For instance, in fig. 13 the underlying  $\bar{\Lambda}_{\overline{\text{MS}}}$  ranges from  $\approx 310$  to  $\approx 390 \text{ MeV}$ . In [77] the authors matched lattice data for the static  $q\bar{q}$  potential to a resummed next-to-next-to-next-leading log perturbative calculation in the perturbative regime  $\simeq 5 \text{ GeV}$  and obtained  $\bar{\Lambda}_{\overline{\text{MS}}} = 315_{-12}^{+18} \text{ MeV}$ . pQCD EOS based on this value is shown as the last column in fig. 13 and is labeled as “lattice”, where the 4-loop running  $\alpha_s$  used throughout [77] is assumed. It is not clear if some of the choices are better than others.

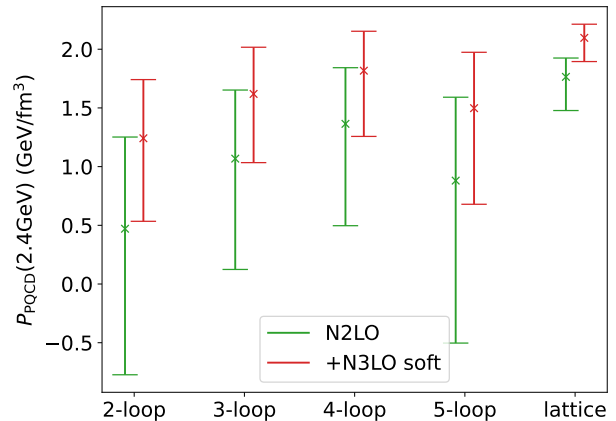


FIG. 13. Pressure of the pQCD EOS with  $X = 1$  at  $\mu_B = 2.4 \text{ GeV}$  obtained with 2-, 3-, 4-, and 5-loop QCD beta functions. The central values and error bars correspond to those of the reference value  $\alpha_s(\bar{\Lambda} = 2 \text{ GeV}) = 0.2994_{-0.0141}^{+0.0152}$ . The last column labeled “lattice” uses the extracted Landau pole from lattice data [77] and is obtained with a 4-loop running (see main text). The 2-loop  $\alpha_s$  adopted in the main text leads to the largest uncertainties, but is consistent with the N2LO pQCD calculation eq. 3. Notice that the effect of the N3LO soft contribution can be significant, and in most cases appear to improve the convergence of pQCD.

## Appendix B: the partial N3LO pQCD EOS

The soft N3LO contribution to the pQCD EOS recently reported in [23, 25] pushes the pressure higher than that predicted by the N2LO result eq. 3, as can be seen in fig. 13. Although this makes eq. 17 more constraining, the main conclusions remain unchanged. For instance, as is shown in fig. 14, the maximally stiff EOSs are still compatible with pQCD predictions assuming  $X = 1$ . Since the maximally stiff inner core EOS predicts the lowest pressure at  $\mu_B \approx 2.2 \text{ GeV}$ , no other valid NS EOSs can be ruled out either. As for the  $\Delta P_{\text{min}}$  bound, the increased  $P_{\text{pQCD}}$  due to soft modes at N3LO renders eq. 12 less constraining. And when eq. 12 is violated the tension becomes weaker, see fig. 15.

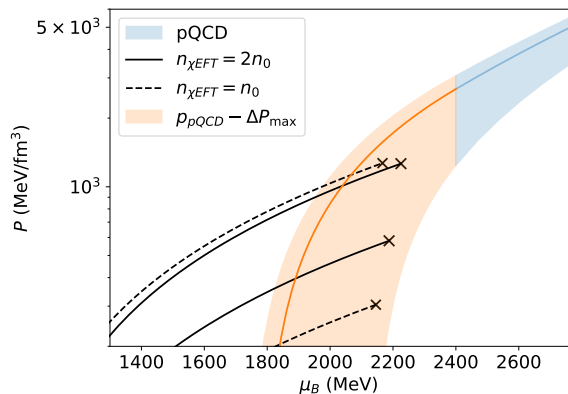


FIG. 14. Similar to fig. 6 except that the partial N3LO contribution is included in the pQCD EOS. None of the NS EOSs are completely ruled out.

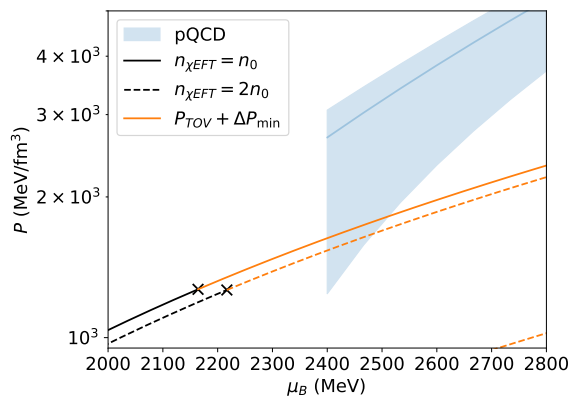


FIG. 15. Similar to fig. 4 except that the partial N3LO contribution is included. The effect of eq. 11 becomes weaker. As explained earlier this is not a constraint on NS EOSs. Since predictions for  $P_{\text{pQCD}}$  at given  $X$  are not expected to be invariant when higher order terms are included in pQCD, and the uncertainties in  $n_{\text{pQCD}}$  are relatively controlled, it is more convenient to directly parameterize pQCD uncertainties in terms of  $P_{\text{pQCD}}$ . For instance, if  $P_{\text{pQCD}}(2.4\text{GeV}) = 1.2\text{ GeV}/\text{fm}^3$  and the maximally soft EOSs are confirmed by astrophysics, assuming the ground state is a CFL phase the pairing gap needs to be at least  $\simeq 100\text{ MeV}$ , see fig. 5.

### Appendix C: incorporating constraints on NS sizes

It has been shown in the main text using both the limiting EOSs and randomly generated samples that (potential) pQCD bounds are orthogonal to those from astrophysical observations. The present section aims to strengthen this statement by explicitly taking into account astrophysical constraints. Specifically, I impose bounds on the tidal deformability of  $1.4M_{\odot}$  stars  $\Lambda_{1.4M_{\odot}} \leq 500$  from GW170817 [78–80], and the putative upper limit  $M_{\text{TOV}} \lesssim 2.3M_{\odot}$  based on speculations that the remnant of GW170817 collapsed to a black hole

within seconds [81, 82]. That the former is orthogonal to pQCD considerations is demonstrated earlier in fig. 7, and that the latter may interfere with pQCD constraints is mainly due to the closer proximity of the TOV limit to  $2M_{\odot}$  stars. All things considered, no appreciable shifts in the observables of  $2M_{\odot}$  stars are found. The same observation holds for the posterior CIs on  $C_s(\mu_B)$  (see figs. 16 and 17) where the effects of pQCD considerations appears to be the strongest.

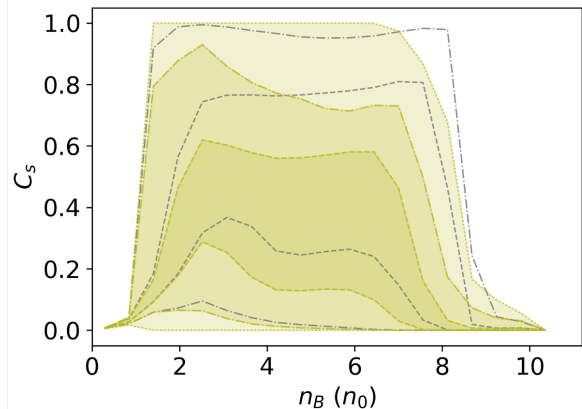


FIG. 16. Similar to fig. 10 except plotted in the  $n_B - C_s$  plane. Notice that the prior CIs shown in black are centered around 0.5 and mostly flat, confirming the peculiar shape seen in fig. 10 is a feature of solutions to the TOV equation instead of an indication of bias. Since the pQCD constraint directly impacts  $C_s(\mu_B)$ , its effects here can be somewhat sensitive to the assumptions underlying the NS EOSs. The results shown here, which drive the CIs lower without introducing additional features, appear to be general and insensitive to those assumptions.

### Appendix D: the number density constraint

The low-density matching points in the  $\Delta P_{\text{min}}$  and  $\Delta P_{\text{max}}$  bounds are taken to be at or below the TOV points of NS EOSs, which vary from one EOS to another. The number density constraint derived in [26] is in a sense a global bound that concerns fixed low- and high-density matching points L and H. The low- and high-density matching points are taken to be  $\mu_{\chi\text{EFT}}$  and  $\mu_{\text{pQCD}}$  in [26]. For all EOSs that pass through an arbitrary point  $(\mu_1, n_1)$  between the two endpoints there exist a maximum and a minimum value of  $\Delta P$ . These limiting cases are shown as the blue and the red curves in fig. 18. By noting the constructions in the density ranges  $[\mu_L, \mu_1]$  and  $[\mu_1, \mu_H]$  are two separate realizations of fig. 3, the expressions for  $\Delta P_{\text{min}}$  and  $\Delta P_{\text{max}}$  can be obtained by replacing the dummy labels in eqs. 10 and 11,



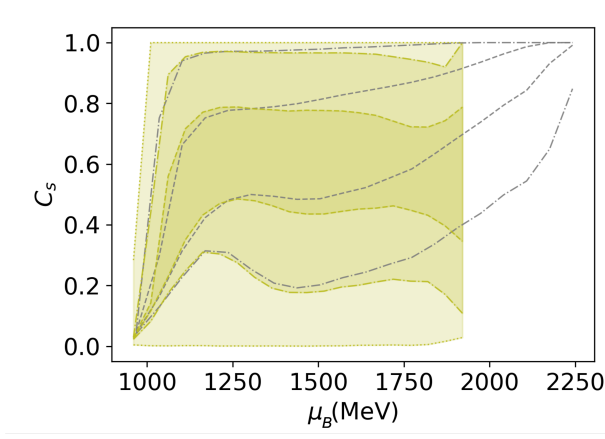


FIG. 17. Similar to fig. 10 but assumes a prior that already incorporates astrophysical constraints  $\Lambda_{1.4M_\odot} \leq 500$  and  $M_{\text{TOV}} \leq 2.3M_\odot$ . When compared to fig. 10, one finds that the astrophysical inputs have negligible effects on  $C_s(\mu_B)$ , even in this hard cutoff approach ignoring astrophysical uncertainties. The pQCD bound once again shifts the CIs on  $C_s$  towards lower values, and forbids  $\mu_{\text{TOV}}$  above  $\approx 1.9$  GeV.

and are

$$\Delta P_{\text{max}} = \frac{n_H \mu_H}{2} \left[ 1 - \left( \frac{\mu_1}{\mu_H} \right)^2 \right] + \frac{n_1 \mu_1}{2} \left[ 1 - \left( \frac{\mu_L}{\mu_1} \right)^2 \right], \quad (\text{D1})$$

$$\Delta P_{\text{min}} = \frac{n_L \mu_L}{2} \left[ \left( \frac{\mu_1}{\mu_L} \right)^2 - 1 \right] + \frac{n_1 \mu_1}{2} \left[ \left( \frac{\mu_H}{\mu_1} \right)^2 - 1 \right]. \quad (\text{D2})$$

In order that there exists an EOS passing through  $(\mu_1, n_1)$ ,  $\Delta P_0 \equiv P_H - P_L$  has to be sandwiched by these limits  $\Delta P_{\text{min}} \leq \Delta P_0 \leq \Delta P_{\text{max}}$ . But as discussed earlier, only the  $\Delta P_{\text{max}}$  bound may be used as a constraint, and it leads to the number density constraint  $n_1(\mu_1) \geq n_{\text{min}}(\mu_1)$  where

$$n_{\text{min}}(\mu) = \frac{2\Delta P_0 - \mu_H n_H \left[ 1 - \left( \frac{\mu}{\mu_H} \right)^2 \right]}{\mu \left[ 1 - \left( \frac{\mu_L}{\mu} \right)^2 \right]}. \quad (\text{D3})$$

This lower limit can be relevant for large  $\mu$  close to  $\mu_H$ , but it blows off near  $\mu_L$ . In fact, it crosses the lower bound eq. 7 (noting that ‘H’ and ‘L’ are just dummy labels there) set by the maximally stiff EOS (blue curve in fig. 18) at

$$\mu_C = \sqrt{\frac{\mu_L \mu_H (\mu_L n_L - \mu_H n_H + 2\Delta P_0)}{\mu_H n_L - \mu_L n_H}}. \quad (\text{D4})$$

Therefore, for baryon chemical potentials below this value  $\mu_C$ , eq. 7

$$n_{\text{min}}(\mu) = \frac{\mu}{\mu_L} n_L \quad (\text{D5})$$

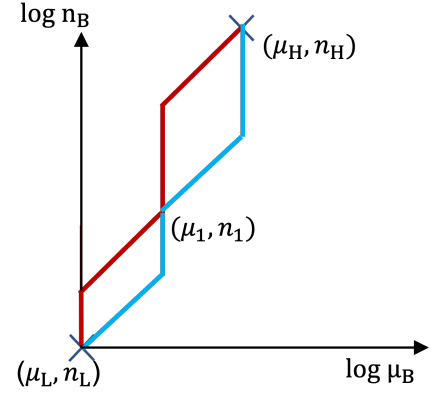


FIG. 18. Schematics for the number density constraint for fixed endpoints and  $\Delta P_0 = P(\mu_H) - P(\mu_L)$ . The curve in blue (red) yields  $\Delta P_{\text{min}}$  ( $\Delta P_{\text{max}}$ ) among all possibilities that pass through the point  $(\mu_1, n_1)$ . These constructions are obtained by stacking two copies of fig. 3 on top of each other.

is the relevant bound.

The  $n_{\text{min}}$  bound is shown in fig. 19 as the dashed, dot-dashed, and dotted lines for  $X = 1, 2, 4$ . The high-density pQCD point is chosen at  $\mu_H = 2.4$  GeV, and the N3LO leading log term in the quark matter EOS is also included. To compare this necessary condition with the one from eq. 17, the limiting NS EOSs modified via the procedure described earlier are shown as the colored solid lines. They are based on the maximally stiff and maximally soft NS EOSs in fig. 6, and are diverted away at the critical points just before eq. 17 is violated via first-order phase transitions. For these extreme models, the integral constraint is identical to the  $\Delta P_{\text{max}}$  bound applied at the critical point. This equivalence can be understood by noting that  $\Delta P_{\text{max}}$  does not depend on  $n_L$ , and the maximally stiff (soft) EOS depicted in blue (red) between  $\mu_L$  and  $\mu_1$  are, plainly, the maximally stiff (soft) inner core EOS shown in fig. 19. In other words, causal and stable NS EOSs automatically satisfy the contributions to  $\Delta P_{\text{max}}$  below  $\mu_1$ . This effectively reduces the problem formulated on the interval  $[\mu_L, \mu_H]$  to that on  $[\mu_1, \mu_H]$ , i.e., fig. 3. For other EOSs that are not maximally stiff or maximally soft, the extreme construction below  $\mu_1$  in fig. 18 suggests that the integral constraint is weaker than the  $\Delta P_{\text{max}}$  bound. For instance, in fig. 19 the solid black curve is required by the  $\Delta P_{\text{max}}$  bound to bend *before* it could violate the integral constraint.

For the sake of completeness, I also provide the expression for  $n_{\text{max}}$  derived from  $\Delta P_{\text{min}} \leq \Delta P_0$ :

$$n_{\text{max}}(\mu) = \frac{2\Delta P_0 - \mu_L n_L \left[ \left( \frac{\mu}{\mu_L} \right)^2 - 1 \right]}{\mu \left[ \left( \frac{\mu_H}{\mu} \right)^2 - 1 \right]}. \quad (\text{D6})$$

It crosses eq. 6 at  $\mu_C$  given by eq. D4, above which it is

replaced by

$$n_{\max}(\mu) = \frac{\mu}{\mu_H} n_H.$$

The  $n_{\max}$  bound is also shown fig. 19 and appears in the upper region. It suggests the maximally soft NS EOSs are incompatible with pQCD predictions assuming  $X = 1$ , and the tension surfaces early on at  $n_{\chi\text{EFT}}$  where first-order phase transitions take place. On one hand, identifying the earliest violation of eq. 12 is a strength of  $n_{\max}$ . On the other hand, for an intuitive view of the non-perturbative effects required to satisfy eq. 12 (or equivalently the  $n_{\max}$  bound), figs. 4 and 15 are better suited.

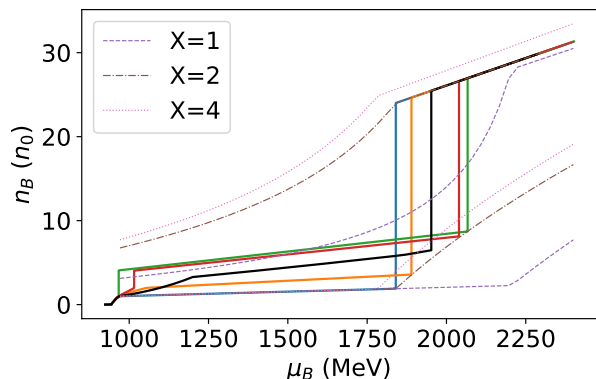


FIG. 19. The number density constraints imposed at  $\mu_{\text{pQCD}} = 2.4$  GeV for  $X = 1, 2, 4$  and at  $\mu_L \approx 970$  MeV (the central value of  $\chi\text{EFT}$  prediction at  $n_0$ ). Soft modes at N3LO are included in the pQCD EOS. The solid colored curves are the modified maximally stiff and maximally soft EOSs compatible with eq. 17. The modification is described in the main text and starts at the critical points shown in fig. 6. The underlying pQCD parameters are identical to those behind the number density constraints shown here except  $X = 2$  only. The outer curves (green and purple) assume  $n_{\chi\text{EFT}} = n_0$  and the inner ones (red and orange) are for  $n_{\chi\text{EFT}} = 2n_0$ . For the limiting EOSs based on  $n_{\chi\text{EFT}} = n_0$ , their critical points sit exactly along the  $n_{\min}$  bound (which assumes the same  $n_L = n_0$  and pQCD parameters). For other EOSs, for example the solid black line, the critical points do not always reach the  $n_{\min}$  bound, demonstrating that the integral constraint is only a necessary condition.

### Appendix E: Model-independent upper bound on $\Delta_{\text{CFL}}$

Here, I report model-independent bounds on the highest  $\Delta_{\text{CFL}}$  allowed by given NS maximum masses. These constraints improve upon the results reported in ref [74] in that they do not require any assumption about NS inner cores.

Taking into account pairing contributions to the EOS eq. 13, the  $\Delta P_{\max}$  bound eq. 17 becomes

$$P_{\text{pQCD}} + P_{\text{CFL}} - P_{\text{TOV}} \leq \Delta P_{\max} \quad (\text{E1})$$

from which one obtains

$$P_{\text{CFL}} \leq \Delta P_{\max} - \Delta P. \quad (\text{E2})$$

The value of  $\Delta_{\text{CFL}}$  can be solved from  $P_{\text{CFL}}$  via eq. 14. For clarity, with the pairing effects included the quantities above are

$$\Delta P_{\max} = \frac{n_{\text{CQM}} \mu_{\text{CQM}}}{2} \left[ 1 - \left( \frac{\mu_{\text{TOV}}}{\mu_{\text{CQM}}} \right)^2 \right]$$

and

$$\Delta P = P_{\text{pQCD}}(\mu_{\text{CQM}}) - P_{\text{TOV}}$$

where  $\mu_{\text{CQM}} \equiv \mu_{\text{pQCD}} \equiv \mu_H$  is the baryon chemical potential at the chosen high-density matching point,  $n_{\text{CQM}}$  is given by eq. 13, and  $P_{\text{pQCD}}(\mu_{\text{CQM}})$  is the perturbative contribution to the pressure.

For chosen pQCD EOS and the high-density matching point, the RHS of eq. E2 is a function of the TOV point and gives an upper bound  $\max\{\Delta_{\text{CFL}}\}$  when the equality holds. It has a global maximum  $\mathbf{max}\{\Delta_{\text{CFL}}\} \equiv \mathbf{max}_{\text{NS}}\{\max\{\Delta_{\text{CFL}}\}\}$  across all NS EOSs reached by the maximally soft NS inner core EOSs. This is because the maximally soft NS EOSs predict the highest  $P_{\text{TOV}}$  at the highest  $\mu_{\text{TOV}}$ . Large  $\Delta_{\text{CFL}}$  yielding  $P_{\text{CQM}}$  too high for the maximally soft NS EOS will certainly overmatch other NS EOSs as well. This upper bound is shown in fig. 20 along with sample-based statistics. The constraints strengthen rapidly with increasing  $X$  near  $X \approx 1$ , largely due to the  $\Delta_{\text{CFL}}^2$  dependence in  $P_{\text{CFL}}$ . In the absence of additional assumptions, the CFL pairing gap at  $\mu_B = 2.4$  GeV can be robustly placed below  $\simeq 500$  MeV by the existence of two-solar-mass pulsars [54–58].

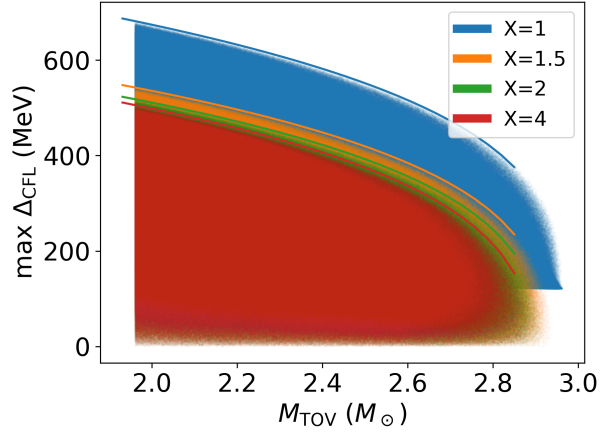


FIG. 20. Maximum allowed CFL pairing gaps as a function of  $M_{\text{TOV}}$ . The dots are computed for each EOS sample by solving  $\Delta_{\text{CFL}}$  that saturates the inequality eq. E2. The lines are based on the maximally soft NS EOSs and give the global upper bound over all NS inner core EOSs. The soft N3LO pQCD contribution to the CQM EOS is included.

- [1] M. Troyer and U.-J. Wiese, Computational complexity and fundamental limitations to fermionic quantum Monte Carlo simulations, *Phys. Rev. Lett.* **94**, 170201 (2005), arXiv:cond-mat/0408370.
- [2] P. de Forcrand, Simulating QCD at finite density, *PoS LAT2009*, 010 (2009), arXiv:1005.0539 [hep-lat].
- [3] D. B. Kaplan, Chiral Symmetry and Lattice Fermions, in *Les Houches Summer School: Session 93: Modern perspectives in lattice QCD: Quantum field theory and high performance computing* (2009) arXiv:0912.2560 [hep-lat].
- [4] W. Baade and F. Zwicky, On super-novae, *Proceedings of the National Academy of Sciences* **20**, 254 (1934).
- [5] S. Weinberg, Nonlinear realizations of chiral symmetry, *Phys. Rev.* **166**, 1568 (1968).
- [6] S. Weinberg, Nuclear forces from chiral Lagrangians, *Phys. Lett. B* **251**, 288 (1990).
- [7] S. Weinberg, Effective chiral Lagrangians for nucleon - pion interactions and nuclear forces, *Nucl. Phys. B* **363**, 3 (1991).
- [8] S. Weinberg, Three body interactions among nucleons and pions, *Phys. Lett. B* **295**, 114 (1992), arXiv:hep-ph/9209257.
- [9] D. B. Kaplan, M. J. Savage, and M. B. Wise, Nucleon - nucleon scattering from effective field theory, *Nucl. Phys. B* **478**, 629 (1996), arXiv:nucl-th/9605002.
- [10] D. B. Kaplan, M. J. Savage, and M. B. Wise, A New expansion for nucleon-nucleon interactions, *Phys. Lett. B* **424**, 390 (1998), arXiv:nucl-th/9801034.
- [11] D. B. Kaplan, M. J. Savage, and M. B. Wise, Two nucleon systems from effective field theory, *Nucl. Phys. B* **534**, 329 (1998), arXiv:nucl-th/9802075.
- [12] S. R. Beane, P. F. Bedaque, M. J. Savage, and U. van Kolck, Towards a perturbative theory of nuclear forces, *Nucl. Phys. A* **700**, 377 (2002), arXiv:nucl-th/0104030.
- [13] T. Krüger, I. Tews, K. Hebeler, and A. Schwenk, Neutron matter from chiral effective field theory interactions, *Phys. Rev. C* **88**, 025802 (2013), arXiv:1304.2212 [nucl-th].
- [14] G. Wlazłowski, J. W. Holt, S. Moroz, A. Bulgac, and K. J. Roche, Auxiliary-field quantum Monte Carlo simulations of neutron matter in chiral effective field theory, *Phys. Rev. Lett.* **113**, 182503 (2014), arXiv:1403.3753.
- [15] S. Gandolfi, A. Lovato, J. Carlson, and K. E. Schmidt, From the lightest nuclei to the equation of state of asymmetric nuclear matter with realistic nuclear interactions, *Phys. Rev. C* **90**, 061306 (2014), arXiv:1406.3388 [nucl-th].
- [16] J. E. Lynn, I. Tews, J. Carlson, S. Gandolfi, A. Gezerlis, K. E. Schmidt, and A. Schwenk, Chiral three-nucleon interactions in light nuclei, neutron- $\alpha$  scattering, and neutron matter (2015), arXiv:1509.03470.
- [17] C. Drischler, K. Hebeler, and A. Schwenk, Chiral interactions up to next-to-next-to-next-to-leading order and nuclear saturation, *Phys. Rev. Lett.* **122**, 042501 (2019), arXiv:1710.08220 [nucl-th].
- [18] C. Drischler, J. A. Melendez, R. J. Furnstahl, and D. R. Phillips, Quantifying uncertainties and correlations in the nuclear-matter equation of state, *Phys. Rev. C* **102**, 054315 (2020), arXiv:2004.07805 [nucl-th].
- [19] B. A. Freedman and L. D. McLerran, Fermions and Gauge Vector Mesons at Finite Temperature and Density. 1. Formal Techniques, *Phys. Rev. D* **16**, 1130 (1977).
- [20] B. A. Freedman and L. D. McLerran, Fermions and Gauge Vector Mesons at Finite Temperature and Density. 3. The Ground State Energy of a Relativistic Quark Gas, *Phys. Rev. D* **16**, 1169 (1977).
- [21] C. Manuel, Hard dense loops in a cold nonAbelian plasma, *Phys. Rev. D* **53**, 5866 (1996), arXiv:hep-ph/9512365.
- [22] A. Kurkela, P. Romatschke, and A. Vuorinen, Cold Quark Matter, *Phys. Rev. D* **81**, 105021 (2010), arXiv:0912.1856 [hep-ph].
- [23] T. Gorda, A. Kurkela, R. Paatelainen, S. Säppi, and A. Vuorinen, Cold quark matter at N<sup>3</sup>LO: Soft contributions, *Phys. Rev. D* **104**, 074015 (2021), arXiv:2103.07427 [hep-ph].
- [24] A. Kurkela and A. Vuorinen, Cool quark matter, *Phys. Rev. Lett.* **117**, 042501 (2016), arXiv:1603.00750 [hep-ph].
- [25] T. Gorda, A. Kurkela, P. Romatschke, S. Säppi, and A. Vuorinen, Next-to-Next-to-Next-to-Leading Order Pressure of Cold Quark Matter: Leading Logarithm, *Phys. Rev. Lett.* **121**, 202701 (2018), arXiv:1807.04120 [hep-ph].
- [26] O. Komoltsev and A. Kurkela, How Perturbative QCD Constrains the Equation of State at Neutron-Star Densities, *Phys. Rev. Lett.* **128**, 202701 (2022), arXiv:2111.05350 [nucl-th].
- [27] T. Gorda, O. Komoltsev, and A. Kurkela, Ab-initio QCD Calculations Impact the Inference of the Neutron-star-matter Equation of State, *Astrophys. J.* **950**, 107 (2023), arXiv:2204.11877 [nucl-th].
- [28] R. Somasundaram, I. Tews, and J. Margueron, Perturbative QCD and the neutron star equation of state, *Phys. Rev. C* **107**, L052801 (2023), arXiv:2204.14039 [nucl-th].
- [29] C. E. Rhoades, Jr. and R. Ruffini, Maximum mass of a neutron star, *Phys. Rev. Lett.* **32**, 324 (1974).
- [30] S. Koranda, N. Stergioulas, and J. L. Friedman, Upper limit set by causality on the rotation and mass of uniformly rotating relativistic stars, *Astrophys. J.* **488**, 799 (1997), arXiv:astro-ph/9608179.
- [31] J. M. Lattimer and M. Prakash, Neutron star structure and the equation of state, *Astrophys. J.* **550**, 426 (2001), arXiv:astro-ph/0002232.
- [32] C. Drischler, S. Han, J. M. Lattimer, M. Prakash, S. Reddy, and T. Zhao, Limiting masses and radii of neutron stars and their implications, *Phys. Rev. C* **103**, 045808 (2021), arXiv:2009.06441 [nucl-th].
- [33] D. Zhou, Bayesian evidence for two peaks in the sound speed in cold dense QCD, (2024), arXiv:2412.08760 [nucl-th].
- [34] J. A. Melendez, R. J. Furnstahl, D. R. Phillips, M. T. Pratala, and S. Wesolowski, Quantifying Correlated Truncation Errors in Effective Field Theory, *Phys. Rev. C* **100**, 044001 (2019), arXiv:1904.10581 [nucl-th].
- [35] M. M. Forbes, S. Bose, S. Reddy, D. Zhou, A. Mukherjee, and S. De, Constraining the neutron-matter equation of state with gravitational waves, *Phys. Rev. D* **100**, 083010 (2019), arXiv:1904.04233 [astro-ph.HE].
- [36] D. Adhikari *et al.* (PREX), Accurate Determination of the Neutron Skin Thickness of <sup>208</sup>Pb through Parity-Violation in Electron Scattering, *Phys. Rev. Lett.* **126**,

- 172502 (2021), arXiv:2102.10767 [nucl-ex].
- [37] B. T. Reed, F. J. Fattoyev, C. J. Horowitz, and J. Piekarewicz, Implications of PREX-2 on the Equation of State of Neutron-Rich Matter, *Phys. Rev. Lett.* **126**, 172503 (2021), arXiv:2101.03193 [nucl-th].
- [38] I. Tews, J. Carlson, S. Gandolfi, and S. Reddy, Constraining the speed of sound inside neutron stars with chiral effective field theory interactions and observations, (2018), arXiv:1801.01923 [nucl-th].
- [39] P. Landry and R. Essick, Nonparametric inference of the neutron star equation of state from gravitational wave observations, *Phys. Rev. D* **99**, 084049 (2019), arXiv:1811.12529 [gr-qc].
- [40] E. Annala, T. Gorda, A. Kurkela, J. Nättilä, and A. Vuorinen, Evidence for quark-matter cores in massive neutron stars, *Nature Phys.* **16**, 907 (2020), arXiv:1903.09121 [astro-ph.HE].
- [41] A. Vuorinen, The Pressure of QCD at finite temperatures and chemical potentials, *Phys. Rev. D* **68**, 054017 (2003), arXiv:hep-ph/0305183.
- [42] A. Ipp and A. Rebhan, Thermodynamics of large  $N(f)$  QCD at finite chemical potential, *JHEP* **06**, 032, arXiv:hep-ph/0305030.
- [43] A. Deur, S. J. Brodsky, and G. F. de Teramond, The QCD Running Coupling, *Nucl. Phys.* **90**, 1 (2016), arXiv:1604.08082 [hep-ph].
- [44] T. Gorda, A. Kurkela, R. Paatelainen, S. Säppi, and A. Vuorinen, Soft Interactions in Cold Quark Matter, *Phys. Rev. Lett.* **127**, 162003 (2021), arXiv:2103.05658 [hep-ph].
- [45] T. Gorda, R. Paatelainen, S. Säppi, and K. Seppänen, Equation of State of Cold Quark Matter to  $O(\alpha_s^3 \ln \alpha_s)$ , *Phys. Rev. Lett.* **131**, 181902 (2023), arXiv:2307.08734 [hep-ph].
- [46] J. Frenkel and J. C. Taylor, High Temperature Limit of Thermal QCD, *Nucl. Phys. B* **334**, 199 (1990).
- [47] E. Braaten and R. D. Pisarski, Soft Amplitudes in Hot Gauge Theories: A General Analysis, *Nucl. Phys. B* **337**, 569 (1990).
- [48] J. C. Taylor and S. M. H. Wong, The Effective Action of Hard Thermal Loops in QCD, *Nucl. Phys. B* **346**, 115 (1990).
- [49] T. Gorda, A. Kurkela, J. Österman, R. Paatelainen, S. Säppi, P. Schicho, K. Seppänen, and A. Vuorinen, Degenerate fermionic matter at N<sup>3</sup>LO: Quantum electrodynamics, *Phys. Rev. D* **107**, L031501 (2023), arXiv:2204.11893 [hep-ph].
- [50] E. Braaten and A. Nieto, Free energy of QCD at high temperature, *Phys. Rev. D* **53**, 3421 (1996), arXiv:hep-ph/9510408.
- [51] E. Braaten and A. Nieto, Effective field theory approach to high temperature thermodynamics, *Phys. Rev. D* **51**, 6990 (1995), arXiv:hep-ph/9501375.
- [52] J. R. Oppenheimer and G. M. Volkoff, On Massive neutron cores, *Phys. Rev.* **55**, 374 (1939).
- [53] R. C. Tolman, Static solutions of Einstein's field equations for spheres of fluid, *Phys. Rev.* **55**, 364 (1939).
- [54] P. Demorest, T. Pennucci, S. Ransom, M. Roberts, and J. Hessels, Shapiro Delay Measurement of A Two Solar Mass Neutron Star, *Nature* **467**, 1081 (2010), arXiv:1010.5788 [astro-ph.HE].
- [55] J. Antoniadis *et al.*, A Massive Pulsar in a Compact Relativistic Binary, *Science* **340**, 6131 (2013), arXiv:1304.6875 [astro-ph.HE].
- [56] H. T. Cromartie *et al.* (NANOGrav), Relativistic Shapiro delay measurements of an extremely massive millisecond pulsar, *Nature Astron.* **4**, 72 (2019), arXiv:1904.06759 [astro-ph.HE].
- [57] R. W. Romani, D. Kandel, A. V. Filippenko, T. G. Brink, and W. Zheng, PSR J1810+1744: Companion Darkening and a Precise High Neutron Star Mass, *Astrophys. J. Lett.* **908**, L46 (2021), arXiv:2101.09822 [astro-ph.HE].
- [58] E. Fonseca *et al.*, Refined Mass and Geometric Measurements of the High-mass PSR J0740+6620, *Astrophys. J. Lett.* **915**, L12 (2021), arXiv:2104.00880 [astro-ph.HE].
- [59] C. Drischler, S. Han, and S. Reddy, Large and massive neutron stars: Implications for the sound speed within QCD of dense matter, *Phys. Rev. C* **105**, 035808 (2022), arXiv:2110.14896 [nucl-th].
- [60] M. G. Alford, K. Rajagopal, and F. Wilczek, QCD at finite baryon density: Nucleon droplets and color superconductivity, *Phys. Lett. B* **422**, 247 (1998), arXiv:hep-ph/9711395.
- [61] D. T. Son, Superconductivity by long range color magnetic interaction in high density quark matter, *Phys. Rev. D* **59**, 094019 (1999), arXiv:hep-ph/9812287.
- [62] M. G. Alford, K. Rajagopal, and F. Wilczek, Color flavor locking and chiral symmetry breaking in high density QCD, *Nucl. Phys. B* **537**, 443 (1999), arXiv:hep-ph/9804403.
- [63] T. Schäfer and F. Wilczek, Superconductivity from perturbative one gluon exchange in high density quark matter, *Phys. Rev. D* **60**, 114033 (1999), arXiv:hep-ph/9906512.
- [64] K. Rajagopal and F. Wilczek, The Condensed matter physics of QCD, in *At the frontier of particle physics. Handbook of QCD. Vol. 1-3*, edited by M. Shifman and B. Ioffe (2000) pp. 2061–2151, arXiv:hep-ph/0011333.
- [65] M. G. Alford, A. Schmitt, K. Rajagopal, and T. Schäfer, Color superconductivity in dense quark matter, *Rev. Mod. Phys.* **80**, 1455 (2008), arXiv:0709.4635 [hep-ph].
- [66] J. Berges and K. Rajagopal, Color superconductivity and chiral symmetry restoration at nonzero baryon density and temperature, *Nucl. Phys. B* **538**, 215 (1999), arXiv:hep-ph/9804233.
- [67] G. W. Carter and D. Diakonov, Light quarks in the instanton vacuum at finite baryon density, *Phys. Rev. D* **60**, 016004 (1999), arXiv:hep-ph/9812445.
- [68] R. D. Pisarski and D. H. Rischke, Gaps and critical temperature for color superconductivity, *Phys. Rev. D* **61**, 051501 (2000), arXiv:nucl-th/9907041.
- [69] J. Braun and B. Schallmo, From quarks and gluons to color superconductivity at supranuclear densities, *Phys. Rev. D* **105**, 036003 (2022), arXiv:2106.04198 [hep-ph].
- [70] D. Zhou, Dwarf (Twin) Neutron Stars I: Did GW170817 Involve One?, (2023), arXiv:2307.13810 [astro-ph.HE].
- [71] D. Zhou, On the parameterization of neutron star equations of state, in preparation (2023).
- [72] L. Fernandez and J.-L. Kneur, All Order Resummed Leading and Next-to-Leading Soft Modes of Dense QCD Pressure, *Phys. Rev. Lett.* **129**, 212001 (2022), arXiv:2109.02410 [hep-ph].
- [73] M. Alford, M. Braby, M. W. Paris, and S. Reddy, Hybrid stars that masquerade as neutron stars, *Astrophys. J.* **629**, 969 (2005), arXiv:nucl-th/0411016.
- [74] A. Kurkela, K. Rajagopal, and R. Steinhorst, Astrophysical Equation-of-State Constraints on the Color-

- Superconducting Gap, (2024), arXiv:2401.16253 [astro-ph.HE].
- [75] P. A. Baikov, K. G. Chetyrkin, and J. H. Kühn, Five-Loop Running of the QCD coupling constant, *Phys. Rev. Lett.* **118**, 082002 (2017), arXiv:1606.08659 [hep-ph].
- [76] R. L. Workman *et al.* (Particle Data Group), Review of Particle Physics, *PTEP* **2022**, 083C01 (2022).
- [77] A. Bazavov, N. Brambilla, X. G. Tormo, I. P. Petreczky, J. Soto, and A. Vairo, Determination of  $\alpha_s$  from the QCD static energy: An update, *Phys. Rev. D* **90**, 074038 (2014), [Erratum: *Phys.Rev.D* 101, 119902 (2020)], arXiv:1407.8437 [hep-ph].
- [78] B. P. Abbott *et al.* (LIGO Scientific, Virgo), GW170817: Measurements of neutron star radii and equation of state, *Phys. Rev. Lett.* **121**, 161101 (2018), arXiv:1805.11581 [gr-qc].
- [79] S. De, D. Finstad, J. M. Lattimer, D. A. Brown, E. Berger, and C. M. Biwer, Constraining the nuclear equation of state with GW170817, *Phys. Rev. Lett.* **121**, 091102 (2018), arXiv:1804.08583 [astro-ph.HE].
- [80] C. D. Capano, I. Tews, S. M. Brown, B. Margalit, S. De, S. Kumar, D. A. Brown, B. Krishnan, and S. Reddy, Stringent constraints on neutron-star radii from multi-messenger observations and nuclear theory, *Nature Astron.* **4**, 625 (2020), arXiv:1908.10352 [astro-ph.HE].
- [81] B. Margalit and B. D. Metzger, Constraining the Maximum Mass of Neutron Stars From Multi-Messenger Observations of GW170817, *Astrophys. J.* **850**, L19 (2017), arXiv:1710.05938 [astro-ph.HE].
- [82] M. Shibata, E. Zhou, K. Kiuchi, and S. Fujibayashi, Constraint on the maximum mass of neutron stars using GW170817 event, *Phys. Rev. D* **100**, 023015 (2019), arXiv:1905.03656 [astro-ph.HE].